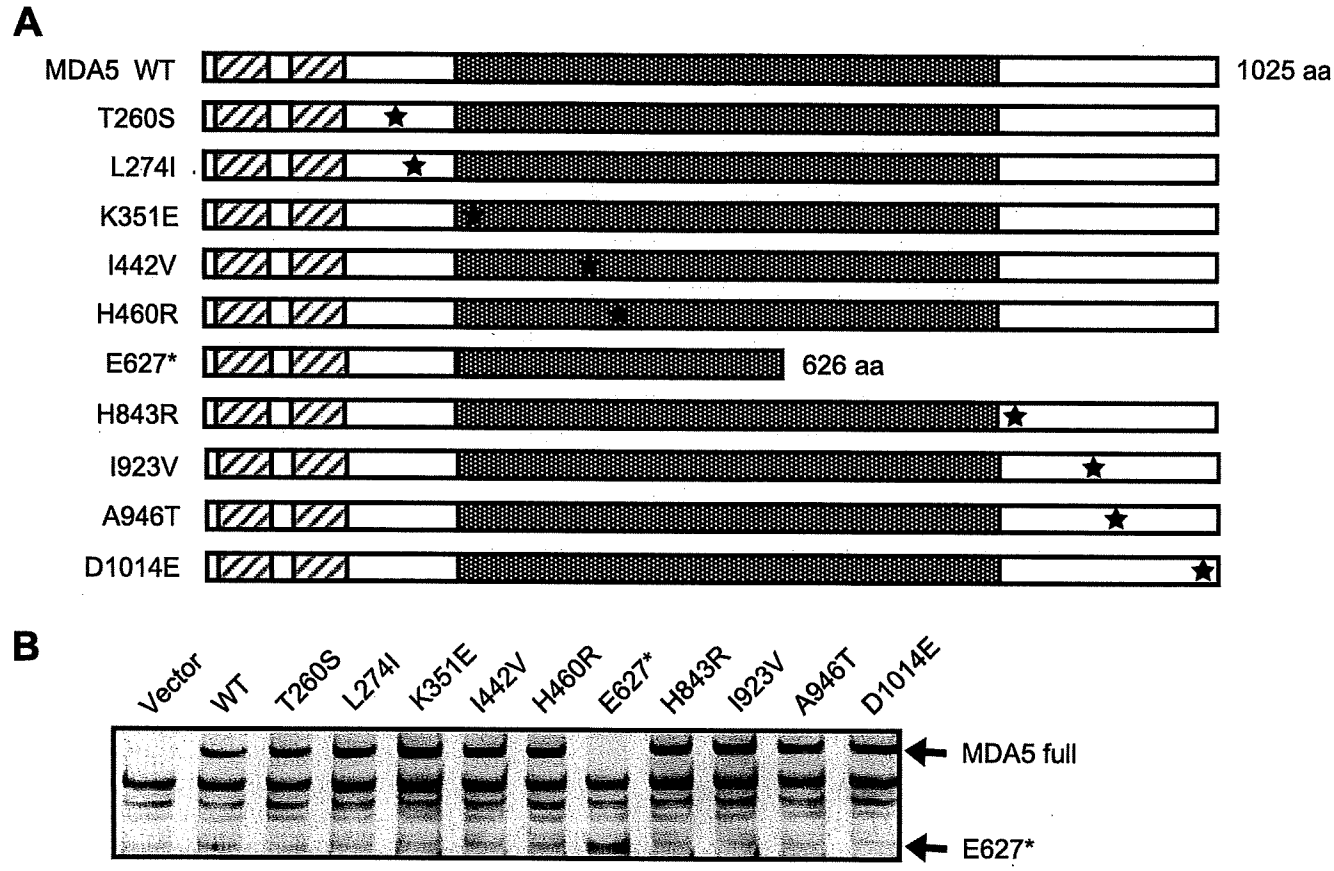

FIGURE 4. **MDA5 nsSNP mutants and their expression in MEFs.** *A*, schematic representation of WT MDA5 and its nsSNPs. Point mutations are indicated by *asterisks*. E627* is the nonsense mutant. *aa*, amino acids. *B*, FLAG-tagged MDA5 SNPs were produced in MDA5$^{-/-}$ MEFs and detected by immunoblotting using an anti-FLAG antibody. *Vector*, empty vector; *MDA5 full*, full-length MDA5.

with the wild type. However, E627* and I923V showed significantly low levels of activity. The phenotypes of these mutations were further tested by transient expression in MDA5$^{-/-}$ MEFs and monitoring endogenous *IFN-β* mRNA (Fig. 5*B*). Although MDA5 is absent, intracellular poly(I-C) induced *IFN-β* gene expression in the control cells (*Vector*). This is presumably due to the activation of RIG-I by a short poly(I-C) present in the preparation we used. Unlike the reporter assay, which monitors only transfected cells, this quantitative PCR assay detects *IFN-β* transcripts from both transfected and non-transfected cells, increasing the background signal. Irrespective of the background, overexpression of WT MDA5 resulted in an enhancement of *IFN-β* expression by poly(I-C), and this induction was not observed with E627* and I923V. Further, the effect was observed at different levels of MDA5 expression. The E627* mutant lacks a part of the helicase domain and the entire CTD in which Ile-923 resides.

Because in the case of RIG-I, the CTD determines RNA recognition specificity, we investigated the RNA binding activity of these mutants by EMSA using ^{32}P-labeled poly(I-C). Wild-type and recombinant MDA5 proteins were expressed in 293T cells and purified. The recombinant proteins were virtually free of other cellular proteins as analyzed by Coomassie Brilliant Blue staining (Fig. 5*C*). Wild-type MDA5 clearly formed a complex with poly(I-C) (Fig. 5*D*), but E627* did not exhibit detectable binding activity. I923V and A946T exhibited activity to bind poly(I-C) as strongly as the wild type under these conditions. We further compared the RNA binding at different protein concentrations (Fig. 5*E*) and confirmed that MDA5 WT and the I923V mutant bind to dsRNA in a comparable fashion. These results suggest that the E627* mutant is biologically inactive due to its failure to recognize its agonist.

DISCUSSION

Human RIG-I Polymorphism—We identified S183I as a loss of function mutation of RIG-I. This serine residue is conserved in human, monkey, cow, and pig RIG-I. The mutation apparently inactivates the tandem CARD, which relays signals downstream. Furthermore, S183I exhibits a dominant inhibitory phenotype, suggesting that individuals retaining this mutation as a heterozygote would exhibit hypersensitivity to viral infections. It has been shown that RIG-I mutants with a CARD deletion (RIG-IC), CARD point mutation (T55I), and ATP-binding site mutation (RIG-I K270A) all function as a dominant inhibitor (3, 7). It has been reported that the repression domain present in the C-terminal region of RIG-I and LGP2 dominantly suppresses the activation of RIG-I in *trans* through interaction with CARD and the helicase loop region (7). Because the repression domain encompasses the RNA-binding domain of RIG-I (6), one mechanism is likely competition of RNA binding with WT RNA. However, the RNA binding-deficient RIG-I mutants, K888A/K907A and K858A/K861A (6), functioned as a dominant negative inhibitor.[3] Interestingly, LGP2 mutants, K643E and K651E, which correspond to Lys-888

[3] J.-P. Zheng and T. Fujita, unpublished observation.

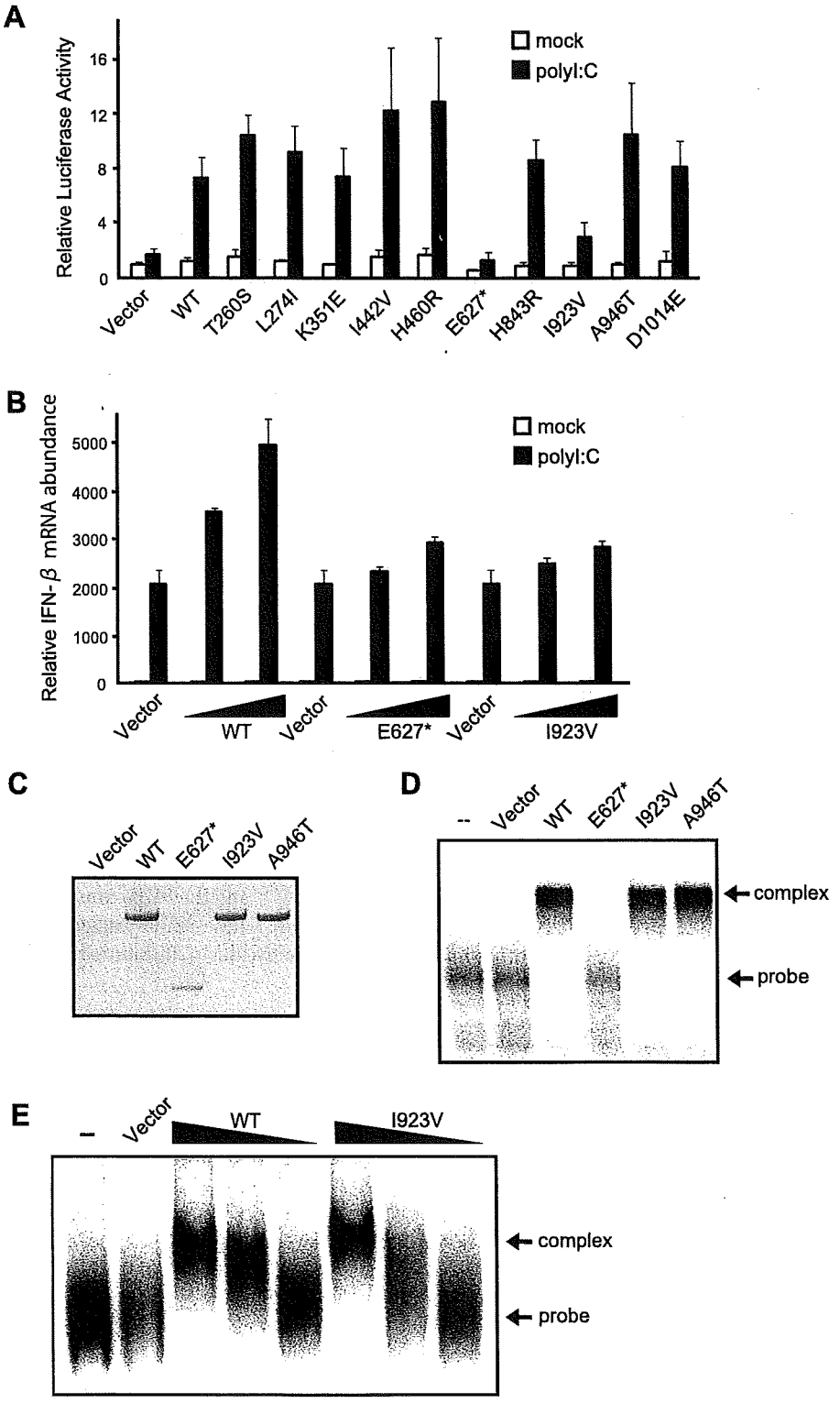

FIGURE 5. **Functional analysis of MDA5 nsSNP mutants.** *A*, MDA5$^{-/-}$ MEFs were transfected with reporter genes together with the indicated constructs as in Fig. 2*A*. After stimulation with poly(I-C) (12 h), the cells were subjected to a Dual-Luciferase assay. *Error bars* show the S.D. values for triplicate transfections. *mock*, mock-treated. *Vector*, empty vector. *B*, MDA5$^{-/-}$ MEFs were transfected with expression vectors for WT MDA5 or E627* or Ile-923 mutants (the total amount of plasmid was kept at 6 μg by adding empty vector). To observe the dose response, cells were transfected with 3 or 5.7 μg of the expression plasmid. Cells were mock-treated or transfected with poly(I-C) for 12 h, and *IFN-β* mRNA was quantified by quantitative PCR as in Fig. 2*C*. *C*, 293T cells were transfected with empty vector, WT MDA5, E627*, I923V, or A946T, and the produced proteins were purified using anti-FLAG ("Experimental Procedures"). The purified proteins were separated by SDS-PAGE and stained by Coomassie Brilliant Blue. *D*, EMSA of the purified MDA5 proteins (500 ng) using ^{32}P-labeled poly(I-C) as a probe. *complex*, probe protein complex; *probe*, free probe. *E*, dose response of RNA binding by WT MDA5 and the I923V mutant. EMSA was performed using 500, 300, and 100 ng of MDA5 and Ile-923 protein.

and Lys-907 of RIG-I, lost RNA binding activity but retain repression function (17). These results strongly suggest an RNA-independent mechanism.

One proposed function of the second CARD is to conjugate to ubiquitin (at Lys-172), which may be essential for signaling activity. However, human RIG-I with K172R, which is resistant to ubiquitination, did not affect phenotype (Fig. 3, *C* and *D*). Moreover, the corresponding amino acid in mouse RIG-I is glutamine, and the corresponding position of MDA5 is glutamic acid (human, monkey, mouse, cow, and pig), suggesting that the ubiquitination of Lys-172 has a minor impact on signaling activity. The precise function of the second CARD is not clear, but a comparative study of Ser-183 and WT RIG-I will elucidate the molecular function of this residue.

Human MDA5 Polymorphism—We identified two loss of function mutations, E627* and I923V, in human MDA5. Each of these mutations is actually present in the human population (13). It is worth investigating the phenotype of the homozygote because *MDA5* knockout mice clearly exhibit hypersusceptibility to the family *Picornaviridae*, genus Cardiovirus. E627*, which lacks CTD and a part of the helicase domain, lost its dsRNA binding activity; hence there was no signaling activity. Although the I923V mutation occurs in the CTD, this mutant exhibited intact dsRNA binding, suggesting a novel function of Ile-923 other than the recognition of RNA. It is worth noting that this• isoleucine is conserved in human, monkey, mouse, cow, and pig MDA5. It is tempting to speculate that Ile-923 participates in an interaction with some other domain of MDA5 or other unknown regulatory protein(s).

A new report by Nejentsev *et al.* (13) describing the relationship between susceptibility to T1D and *MDA5* polymorphism was published. The report describes that four rare mutations (two mutations

in the exon and two mutations in the intron) in the human *MDA5* gene are associated with protection against T1D. Our analysis included the two exon mutations (E627* and I923V), which exhibited a loss of function phenotype. The genetic analysis included another rare nsSNP, H460R, shown to be independent of T1D resistance. The phenotype of this mutant was normal in our analysis. On the other hand, A946T, which was suggested to associate with T1D in previous reports (13, 16), did not exhibit a loss of function phenotype. However, because Nejentsev *et al.* (13) suggested that the association of A946R with T1D was due to the effect of another nsSNP, R843H, a combination of these mutations might confer loss of function on MDA5. In summary, our analysis strongly suggests that loss of function mutations of MDA5 have a causative role in resistance to T1D. Although T1D has a complex pathology, these findings may provide a new strategy for establishing an animal model for T1D.

The human genome encodes multiple sensors, including TLRs and RLRs for viral PAMPs. Some of these may act redundantly to secure defense against viral infections. In the case of RLRs, RIG-I and MDA5 detect a distinct spectrum of viruses, as suggested from the phenotype of respective knock-out mice. There is variation within human populations in susceptibility to a particular viral infection. We argue for a possible contribution of the genetic diversity of RLRs, including those identified in the current investigation, to susceptibility. In addition to the impact of the infection itself, secondary effects such as autoimmunity, which is remotely triggered by certain viral infections, may be influenced at least in part through the functional diversity of RLRs. In summary, our results suggest a critical relationship between RLR polymorphisms and diseases including viral infections and autoimmunity.

Acknowledgments—We greatly appreciate the gift of MEFs from Dr. S. Akira (Research Institute for Microbial Diseases, Osaka University, Osaka). We give our thanks to Dr. F. Matsuda (Center for Genomic Medicine, Kyoto University, Kyoto) for discussion.

REFERENCES

1. Samuel, C. E. (2001) *Clin. Microbiol. Rev.* **14,** 778–809
2. Akira, S., Uematsu, S., and Takeuchi, O. (2006) *Cell* **124,** 783–801
3. Yoneyama, M., Kikuchi, M., Natsukawa, T., Shinobu, N., Imaizumi, T., Miyagishi, M., Taira, K., Akira, S., and Fujita, T. (2004) *Nat. Immun.* **5,** 730–737
4. Yoneyama, M., and Fujita, T. (2008) *Immunity* **29,** 178–181
5. Cui, S., Eisenacher, K., Kirchhofer, A., Brzozka, K., Lammens, A., Lammens, K., Fujita, T., Conzelmann, K. K., Krug, A., and Hopfner, K. P. (2008) *Mol. Cell* **29,** 169–179
6. Takahasi, K., Yoneyama, M., Nishihori, T., Hirai, R., Kumeta, H., Narita, R., Gale, M., Jr., Inagaki, F., and Fujita, T. (2008) *Mol. Cell* **29,** 428–440
7. Saito, T., Hirai, R., Loo, Y. M., Owen, D., Johnson, C. L., Sinha, S. C., Akira, S., Fujita, T., and Gale, M., Jr. (2007) *Proc. Natl. Acad. Sci. U. S. A.* **104,** 582–587
8. Gitlin, L., Barchet, W., Gilfillan, S., Cella, M., Beutler, B., Flavell, R. A., Diamond, M. S., and Colonna, M. (2006) *Proc. Natl. Acad. Sci. U. S. A.* **103,** 8459–8464
9. Kato, H., Takeuchi, O., Sato, S., Yoneyama, M., Yamamoto, M., Matsui, K., Uematsu, S., Jung, A., Kawai, T., Ishii, K. J., Yamaguchi, O., Otsu, K., Tsujimura, T., Koh, C. S., Reis e Sousa, C., Matsuura, Y., Fujita, T., and Akira, S. (2006) *Nature* **441,** 101–105
10. Hornung, V., Ellegast, J., Kim, S., Brzozka, K., Jung, A., Kato, H., Poeck, H., Akira, S., Conzelmann, K. K., Schlee, M., Endres, S., and Hartmann, G. (2006) *Science* **314,** 994–997
11. Kato, H., Takeuchi, O., Mikamo-Satoh, E., Hirai, R., Kawai, T., Matsushita, K., Hiiragi, A., Dermody, T. S., Fujita, T., and Akira, S. (2008) *J. Exp. Med.* **205,** 1601–1610
12. Pichlmair, A., Schulz, O., Tan, C. P., Naslund, T. I., Liljestrom, P., Weber, F., and Reis e Sousa, C. (2006) *Science* **314,** 997–1001
13. Nejentsev, S., Walker, N., Riches, D., Egholm, M., and Todd, J. A. (March 5, 2009) *Science* 10.1126/science.1167728
14. Yoneyama, M., Kikuchi, M., Matsumoto, K., Imaizumi, T., Miyagishi, M., Taira, K., Foy, E., Loo, Y. M., Gale, M., Jr., Akira, S., Yonehara, S., Kato, A., and Fujita, T. (2005) *J. Immunol.* **175,** 2851–2858
15. Gack, M. U., Shin, Y. C., Joo, C. H., Urano, T., Liang, C., Sun, L., Takeuchi, O., Akira, S., Chen, Z., Inoue, S., and Jung, J. U. (2007) *Nature* **446,** 916–920
16. Smyth, D. J., Cooper, J. D., Bailey, R., Field, S., Burren, O., Smink, L. J., Guja, C., Ionescu-Tirgoviste, C., Widmer, B., Dunger, D. B., Savage, D. A., Walker, N. M., Clayton, D. G., and Todd, J. A. (2006) *Nat. Genet.* **38,** 617–619
17. Li, X., Ranjith-Kumar, C. T., Brooks, M. T., Dharmaiah, S., Herr, A. B., Kao, C., and Li, P. (March 28, 2009) *J. Biol. Chem.* 10.1074/jbc.M900818200

THE JOURNAL OF BIOLOGICAL CHEMISTRY VOL. 284, NO. 26, pp. 17465–17474, June 26, 2009

Solution Structures of Cytosolic RNA Sensor MDA5 and LGP2 C-terminal Domains

IDENTIFICATION OF THE RNA RECOGNITION LOOP IN RIG-I-LIKE RECEPTORS[*][S]

Received for publication, January 12, 2009, and in revised form, April 11, 2009 Published, JBC Papers in Press, April 20, 2009, DOI 10.1074/jbc.M109.007179

Kiyohiro Takahasi[‡], Hiroyuki Kumeta[‡], Natsuko Tsuduki[‡], Ryo Narita[§¶], Taeko Shigemoto[§¶], Reiko Hirai[§¶], Mitsutoshi Yoneyama[§¶‖], Masataka Horiuchi[‡], Kenji Ogura[‡], Takashi Fujita[§¶], and Fuyuhiko Inagaki[‡1]

From the [‡]Department of Structural Biology, Graduate School of Pharmaceutical Sciences, Hokkaido University, N-21, W-11, Kita-ku, Sapporo 001-0021, the [§]Laboratory of Molecular Genetics, Institute for Virus Research, Kyoto University, Kyoto 606-8507, the [¶]Laboratory of Molecular Cell Biology, Graduate School of Biostudies, Kyoto University, Kyoto 606-8507, and [‖]PRESTO, Japan Science and Technology Agency, 4-1-8 Honcho Kawaguchi, Saitama 332-0012, Japan

The RIG-I like receptor (RLR) comprises three homologues: RIG-I (retinoic acid-inducible gene *I*), MDA5 (melanoma differentiation-associated gene *5*), and LGP2 (laboratory of genetics and physiology *2*). Each RLR senses different viral infections by recognizing replicating viral RNA in the cytoplasm. The RLR contains a conserved C-terminal domain (CTD), which is responsible for the binding specificity to the viral RNAs, including double-stranded RNA (dsRNA) and 5′-triphosphated single-stranded RNA (5′ppp-ssRNA). Here, the solution structures of the MDA5 and LGP2 CTD domains were solved by NMR and compared with those of RIG-I CTD. The CTD domains each have a similar fold and a similar basic surface but there is the distinct structural feature of a RNA binding loop; The LGP2 and RIG-I CTD domains have a large basic surface, one bank of which is formed by the RNA binding loop. MDA5 also has a large basic surface that is extensively flat due to open conformation of the RNA binding loop. The NMR chemical shift perturbation study showed that dsRNA and 5′ppp-ssRNA are bound to the basic surface of LGP2 CTD, whereas dsRNA is bound to the basic surface of MDA5 CTD but much more weakly, indicating that the conformation of the RNA binding loop is responsible for the sensitivity to dsRNA and 5′ppp-ssRNA. Mutation study of the basic surface and the RNA binding loop supports the conclusion from the structure studies. Thus, the CTD is responsible for the binding affinity to the viral RNAs.

A variety of pathogen-associated molecular patterns, including microbial peptidoglycan, lipopolysaccharide, β-1,3-glucan, and viral DNA or RNA are recognized by pattern recognition receptors that evoke the innate immune responses of host cells. In viral infections, double-stranded RNA (dsRNA)[2] is recognized by Toll-like receptor-3 in the early endosome and by RIG-I like receptors (RLRs) in the cytoplasm. These two receptors initiate the innate immune responses including the production of cytokines and type-I interferon, which are critical for the subsequent adaptive immune response (1).

The RLR comprises three homologs: RIG-I (retinoic acid-inducible gene *I*), MDA5 (melanoma differentiation-associated gene *5*), and LGP2 (laboratory of genetics and physiology *2*) (see Fig. 1*A*) (2), and they sense a viral infection by recognizing replicating viral RNA in the cytoplasm. The RIG-I and MDA5 consist of three functional domains: tandem-CARDs (caspase activation and recruitment domain), a DEAD box helicase-like domain, and a well conserved C-terminal domain (CTD), whereas LGP2 has only the DEAD box helicase like domain and well conserved CTD. The three RLRs are considered to play different roles in the recognition of pathogen-associated molecular patterns and to be activated by different viruses and different viral RNAs. RIG-I is activated by a variety of viruses, including paramyxovirus, rhabdovirus, and orthomyxovirus, recognizing not only dsRNA but also 5′-triphosphated single-stranded RNA (5′ppp-ssRNA) (3, 4), and MDA5 is mainly activated by picornavirus (5, 6), whereas LGP2 lacking the tandem CARDs was originally identified as a negative regulator, but gene disruption study showed that it may function as a positive regulator (2, 7).

Our previous study has shown that the three domains of RIG-I cooperatively take part in pathogen-associated molecular pattern recognition and signal transduction (8). Further, the tandem CARDs are essential to transduce the signal via CARD-CARD interaction with the downstream CARD containing signal element, IPS-1/MAVS/VISA/Cardif (9–12). The CTD plays a critical role in the specific recognition of dsRNA and

* This work was supported by grants-in-aid (Tokutei-ryoiki (Matrix of Infection Phenomena), Kiban (S)) and National Projects on Targeted Proteins Research Program from the Japanese Ministry of Education, Culture, Sports, Science, and Technology, by a Research Grant of the Uehara Memorial Foundation, and by Nippon Boehringer Ingelheim Co., Ltd.

The atomic coordinates and structure factors (codes 2RQB and 2RQA) have been deposited in the Protein Data Bank, Research Collaboratory for Structural Bioinformatics, Rutgers University, New Brunswick, NJ (http://www.rcsb.org/).

[S] The on-line version of this article (available at http://www.jbc.org) contains supplemental Figs. 1–4 and supplemental Table 1.

[1] To whom correspondence should be addressed: Dept. of Structural Biology, Graduate School of Pharmaceutical Sciences, Hokkaido University, N-21, W-11, Kita-ku, Sapporo 001-0021, Japan. Tel.: 81-11-706-9011; Fax: 81-11-706-9012; E-mail: finagaki@pharm.hokudai.ac.jp.

[2] The abbreviations used are: dsRNA, double-stranded RNA; ssRNA, single-stranded RNA; RLR, RIG-I-like receptor; CARD, caspase recruitment domain; IPS-1, interferon promoter stimulator-1; RIG-I, retinoic acid-inducible gene *I*; MDA5, melanoma differentiation-associated gene *5*; LGP2, laboratory of genetics and physiology 2; 5′ppp-ssRNA, 5′-triphosphated single-stranded RNA; GST, glutathione *S*-transferase; CTD, C-terminal domain; PBS, phosphate-buffered saline; Bis-Tris, 2-[bis(2-hydroxyethyl)amino]-2-(hydroxymethyl)propane-1,3-diol; DTT, dithiothreitol; NOESY, nuclear Overhauser effect spectroscopy; wt, wild type; EMSA, electrophoretic mobility shift assay; SPR, surface plasmon resonance.

5′ppp-ssRNA, while the DEAD box helicase cooperatively enhances the affinity to dsRNA through a conformational change. In the resting state, RIG-I is believed to be in closed conformation via interaction with these three domains (13). Upon viral infection, CTD specifically recognizes viral RNA and induces a domain rearrangement that allows RIG-I to form a stable complex with viral RNA and simultaneously exposes the tandem CARDs so that RIG-I is assumed to become an open conformation to interact with IPS-1/MAVS/VISA/Cardif (8, 14).

In the previous report, we have solved the solution structure of RIG-I CTD and shown the presence of a large positively charged surface that is responsible for viral RNA binding. In this report, we compare RNA-binding activity of the three CTDs (RIG-I, MDA5, and LGP2) and determine the solution structures of MDA5 and LGP2 CTDs. The RNA-binding activity is correlated to a conserved RNA binding loop, including a critical phenylalanine residue of RIG-I and LGP2. This residue is not conserved in MDA5, reflecting the distinct specificity of this sensor. Our results provide new insights into the recognition of viral RNA in cytoplasm.

EXPERIMENTAL PROCEDURES

Recombinant Proteins—The C-terminal domains of human MDA5 (896–1025) and LGP2 (546–678) were amplified by PCR and inserted into a pGEX-6P-1 vector to produce GST fusion protein (Amersham Biosciences). Expression vectors were introduced into *Escherichia coli* BL21(DE3) cells and cultured in M9 medium. The MDA5 CTD expression was induced by addition of 0.01 mM isopropyl 1-thio-β-D-galactopyranoside when the absorbance at 600 nm was ~0.4. The cells were then grown at 16 °C for 20 h; LGP2 CTD expression was induced by 1 mM isopropyl 1-thio-β-D-galactopyranoside then incubated at 25 °C for 20 h. The cells were suspended in PBS containing 1 mM 4-(2-aminoethyl)benzenesulfonylfluoride hydrochloride, lysed via sonication, and centrifuged. The supernatant was mixed with glutathione-Sepharose 4B (Amersham Biosciences) for 12 h, and the protein bound to glutathione-Sepharose 4B was washed first with PBS then with PBS containing 500 mM NaCl to remove the nucleic acid bound to the protein. The proteins were eluted with 50 mM Tris, pH 8, 150 mM NaCl, 20 mM reduced glutathione. The eluted protein was digested by PreScission protease (Amersham Biosciences). The proteins were further purified with size-exclusion Superdex 75 columns (Amersham Biosciences) with PBS containing 500 mM NaCl.

Site-directed Mutagenesis and Preparation of Mutant Proteins Using 293T Cells—Mutations of the RLR were introduced by the overlap extension PCR (15). The mutagenized cDNA, which was designed to possess an N-terminal FLAG tag, was subcloned into pEFBOS. The expression vectors were transiently transfected to 293T cells and purified by anti FLAG beads (8). The mutations did not alter the stability of the RLR proteins drastically as the production levels, and the recoveries from the transfected mammalian cells are comparable (Figs. 5–7).

Preparation of Uniformly Labeled Proteins—Uniformly Labeled MDA5 and LGP2 CTDs were expressed as above except here using medium containing ^{15}N-ammonium chloride and D-glucose (or [D-^{13}C]glucose), and purified similarly. The NMR samples for the structure determination were prepared at 0.94 mM MDA5 CTD in 20 mM Bis-Tris, pH 7.0, 250 mM NaCl, 10 mM DTT, and 1.00 mM LGP2 CTD in 50 mM Tris, pH 7, 250 mM NaCl, and 1 mM DTT.

NMR Measurements—The NMR spectra were acquired at 25 °C on Varian Unity Inova 500, 600, and 800 spectrometers. The data were processed using NMRPipe (16) and analyzed using Sparky (T. D. Goddard and D. G. Kneller, SPARKY 3, University of California, San Francisco). For assignments of the protein backbone and side-chain ^{1}H, ^{15}N, and ^{13}C resonances, two- and three-dimensional (2D and 3D) spectra were obtained. Backbone resonances were assigned using the 2D ^{1}H-^{15}N HSQC, 3D HNCA, HN(CO)CA, HNCACB, CBCA(CO)NH, HNCO, (HCA)CO(CA)NH, HNCAHA, and HBHA(CO)NH spectra. The aliphatic atoms of the side chains were assigned using 2D ^{1}H-^{13}C HSQC, 3D C(CO)NH, H(CCO)NH, CCH-TOCSY, and HCCH-TOCSY spectra, while aromatic side-chain atoms were assigned using the 2D ^{1}H-^{13}C HSQC, (Hb)Cb(CgCd)Hd, (Hb)Cb(CgCdCe)He, and 3D HCCH-TOCSY spectra.

Structural Determination—The 3D ^{15}N-edited NOESY and ^{13}C-edited NOESY spectra (t_{mix} = 80 ms) were measured to

TABLE 1
Structural statistics for 20 MDA5 CTD

NOE distance constraints	
Total	2970
Short range |i-j|< = 1	1662
Medium range 1<|i-j|<5	372
Long range |i-j|> = 5	982
Dihedral angle constraints	
ϕ	76
ψ	73
Residual NOE violations	
Number > 0.3 Å	0
Residual angle violations	
Number > 5.0°	0
Ramachandran statistics (%)	
Residues in most favored region	74.0
Residues in additionally allowed region	24.1
Residues in generally allowed region	1.9
Residues in disallowed region	0
Structural coordinates root mean square deviation (Å) (residues 897–1017)	
Backbone atoms for the final ensemble	0.40
All heavy atoms for the final ensemble	0.76

TABLE 2
Structural statistics for 20 LGP2 CTD

NOE distance constraints	
Total	2593
Short range |i-j|< = 1	1517
Medium range 1<|i-j|<5	322
Long range |i-j|> = 5	754
Dihedral angle constraints	
ϕ	58
ψ	62
Residual NOE violations	
Number > 0.3 Å	2
Residual angle violations	
Number > 5.0°	0
Ramachandran statistics (%)	
Residues in most favored region	71.0
Residues in additionally allowed region	27.4
Residues in generally allowed region	1.7
Residues in disallowed region	0
Structural coordinates root mean square deviation (Å) (residues 549–657)	
Backbone atoms for the final ensemble	0.49
All heavy atoms for the final ensemble	0.84

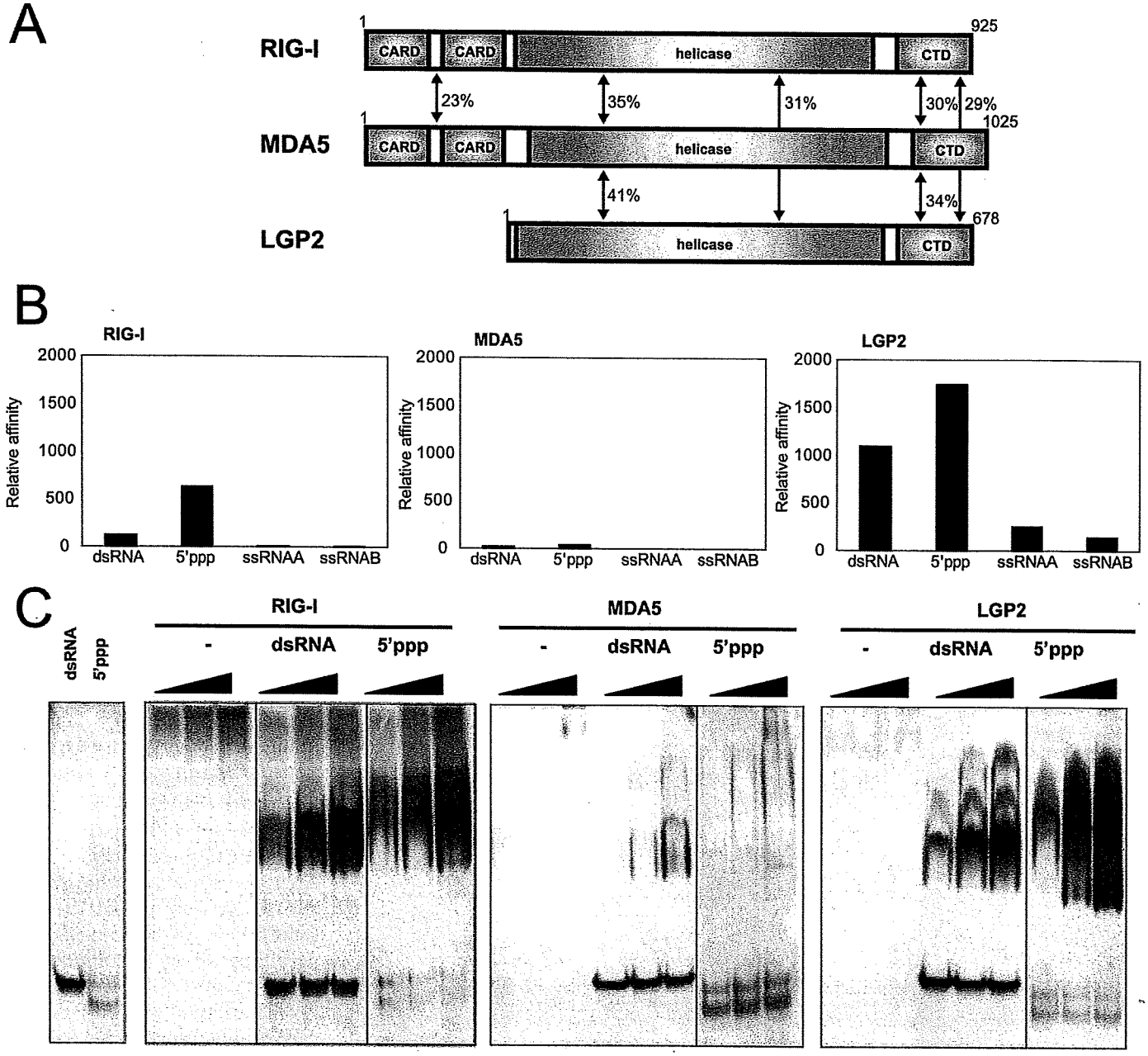

FIGURE 1. **Functional analysis of RLR CTDs.** *A*, domain structures of RIG-I, MDA5, and LGP2. Sequence identities of each domain among the RLRs are indicated. *B*, RNA-binding activity of RLR CTDs determined by SPR. GST-RIG-I CTD, GST-MDA5 CTD, and GST-LGP2 CTD were captured by the anti-GST anti-body immobilized onto the sensor chip, then dsRNA, 5′ppp-ssRNA, and two ssRNAs (*ssRNAA* and *ssRNAB*) were injected. Each resonance unit of RNA bound to a GST fused protein are standardized by molecular weight of the RNAs, then normalized by the resonance unit and molecular weight of the captured GST-fused protein. Normalized data are summarized and shown as *bar graphs*. RNAs bound to RIG-I, MDA5, and LGP2 are indicated from *left* to *right* in the *panels*. *C*, RNA-binding activity of RLR CTDs determined by EMSA. CTDs without the GST tag were prepared and subjected to EMSA. Increasing amounts of CTD (10, 20, and 40 pm) were reacted with the indicated probe and analyzed by native PAGE. The gels were silver-stained to visualize protein and RNA probe. −, no RNA; *dsRNA*, 25/25c probe; *5′ppp*: 5′pppGG25 probe.

obtain NOE distance constraints. Backbone ϕ and ψ dihedral angle constraints were generated using the TALOS program (17). The structures of MDA5 CTD and LGP2 CTD were determined using CANDID/CYANA 2.1 (18, 19). Structural statistics for the best 20 structures of MDA5 CTD and LGP2 CTD are shown in Tables 1 and 2. The 20 lowest energy structures of both MDA5 CTD and LGP2 CTD were deposited at the Protein Data Bank (PDB codes 2RQB and 2RQA, respectively).

NMR Titration Study of LGP2—The chemical shift perturbation study of the amide nitrogen and proton signals of LGP2 CTD in ^{1}H-^{15}N HSQC spectra was performed upon addition of the following RNAs: GG25/2 + 25c (dsRNA), 5′-triphosphated GG25 (5′ppp-ssRNA), two single-stranded RNAs GG25 (ssRNAA), and 2 + 25C (ssRNAB) were also titrated as controls. The GG25/2 + 25c was prepared by mixing equal molar GG25 and 2 + 25c, and then annealed in 1×M buffer (10 mM Tris, pH 7.5, 10 mM $MgCl_2$, 1 mM DTT). The final concentration of dsRNA was 0.71 mM. To equalize the condition of the titration experiments, GG25, 2 + 25C, and 5′-triphosphated GG25 was prepared at 0.71 mM in 1×M

Solution Structures of MDA5 CTD and LGP2 CTD

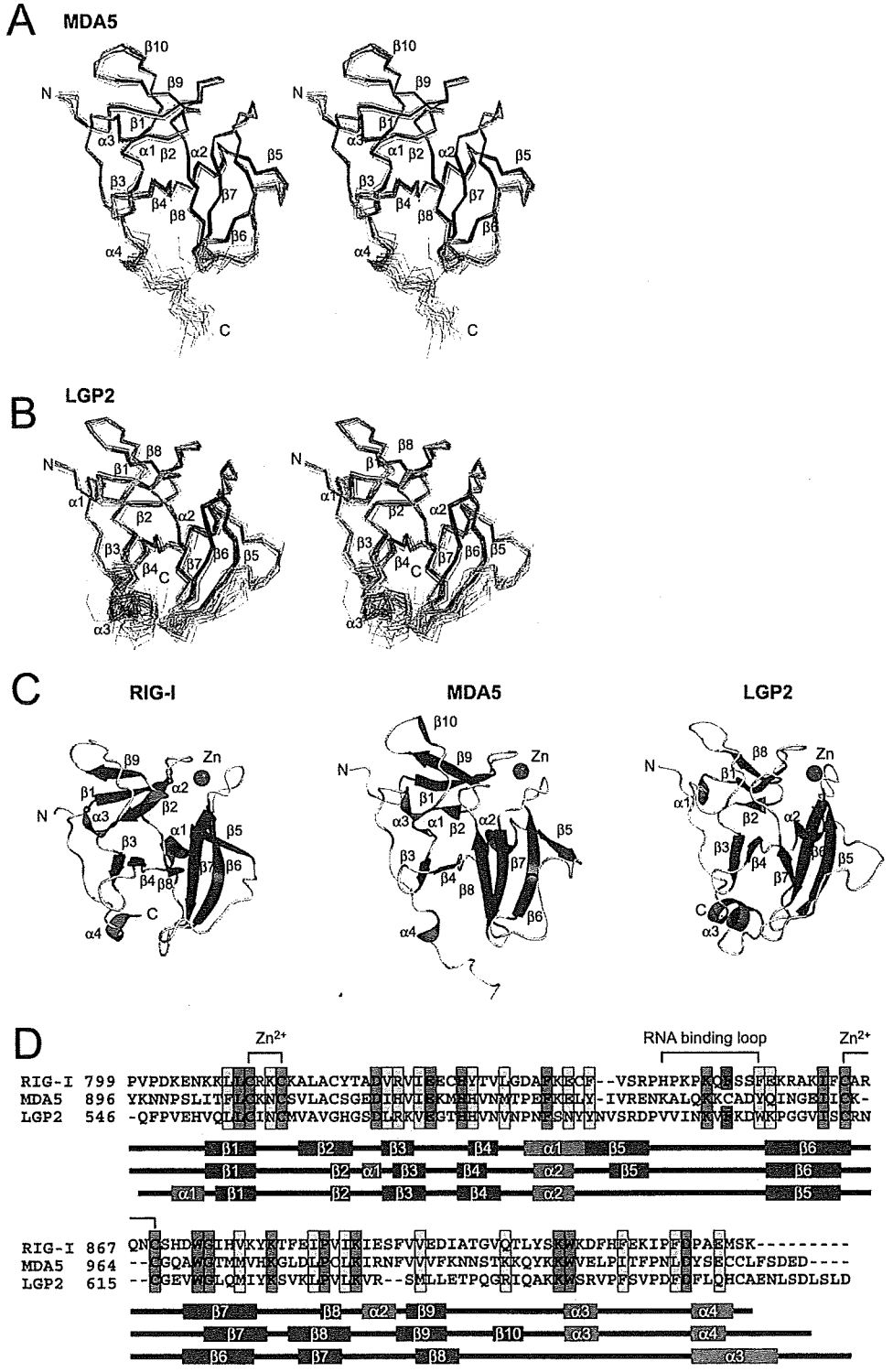

FIGURE 2. **Solution structure of MDA5 CTD and LGP2 CTD.** *A* and *B*, best fit superposition of the backbone atoms of 20 NMR-derived MDA5 CTD (*A*) and LGP2 CTD (*B*). Structures are shown in stereo. β-Strands and α-helices are shown in *blue* and *red*, respectively. *C*, *ribbon diagrams* of the structure of RIG-I CTD, MDA5 CTD, and LGP2 CTD (*left* to *right*). Secondary structure elements are labeled. The figure was prepared using PyMOL. *D*, sequence alignment of human RIG-I, MDA5, and LGP2 CTDs. ClustalX was used to align the sequences. The secondary structure elements of each CTD are indicated below the alignment. The amino acids in *red* and *yellow* indicate conserved (*red*) and type-conserved (*yellow*) residues with the Zn^{2+} binding Cys-*X*-*X*-Cys motifs and RNA binding loop. The Phe residues conserved in RIG-I and LGP2 in the RNA binding loop are colored *green*.

buffer. The ^{15}N-labeled LGP2 CTD was prepared at 92.4 μM in 250 μl of 50 mM Tris, pH 7, 250 mM NaCl, 1 mM DTT, and 10% D_2O. The volume of RNA at the addition of 1.0 equivalent molar ratio was 32.5 μl. 1×M buffer alone was also titrated, and it was confirmed that there was no effect on the NMR spectrum by the buffer. GG25, 5′-GGAAACUAAAAGGGAGAAGUGAAAGUG-3′; 2 + 25C, 5′-AUCACUUUCACUUCUCCCUUUCAGUUU-3′.

NMR Titration Study of MDA5—The experiment was performed in the same manner as in the study of LGP2 except for slightly different conditions of RNA and protein concentrations. Final concentration of RNAs were 0.644 mM, and the MDA5 CTD was prepared at 105 μM in 250 μl of 50 mM Tris, pH 7, 250 mM NaCl, 1.5 mM DTT, and 10% D_2O. The volume of RNA at the addition of 1.0 equivalent molar ratio was 40.8 μl.

Surface Plasmon Resonance Analysis—A Biacore X (Amersham Biosciences) was used for the SPR study. First, GST-fused RIG-I, MDA5, and LGP2 CTD were trapped by anti-GST antibody immobilized on the surface of a sensor CM4 chip, then RNAs were injected to detect the interaction. The standard running buffer used in the analysis was 50 mM Tris, pH 7.5, 150 mM NaCl, and the proteins and RNAs were prepared in the same buffer. All experiments were performed at 25 °C. Immobilization of anti-GST antibody and regeneration of the surface was carried out using a GST Capture Kit and an Amine Coupling Kit (Amersham Biosciences) according to the instruction manuals. The GST-RLR CTDs were prepared at 20 μg/ml and injected for 300 s at the flow rate of 20 μl/min confirming the amount of CTDs captured to the anti-GST antibody with the Resonance Unit (RU) to be ~800. As a control, GST was captured in an anti-GST antibody immobilized reference cell. The RNAs (dsRNA, 5′ppp-ssRNA, ssRNAA, and ssRNAB) were prepared at 1 μM and injected for 120 s at the flow rate of 20 μl/min and data were acquired as the difference in RU between GST-RLR CTDs captured cells and reference cells.

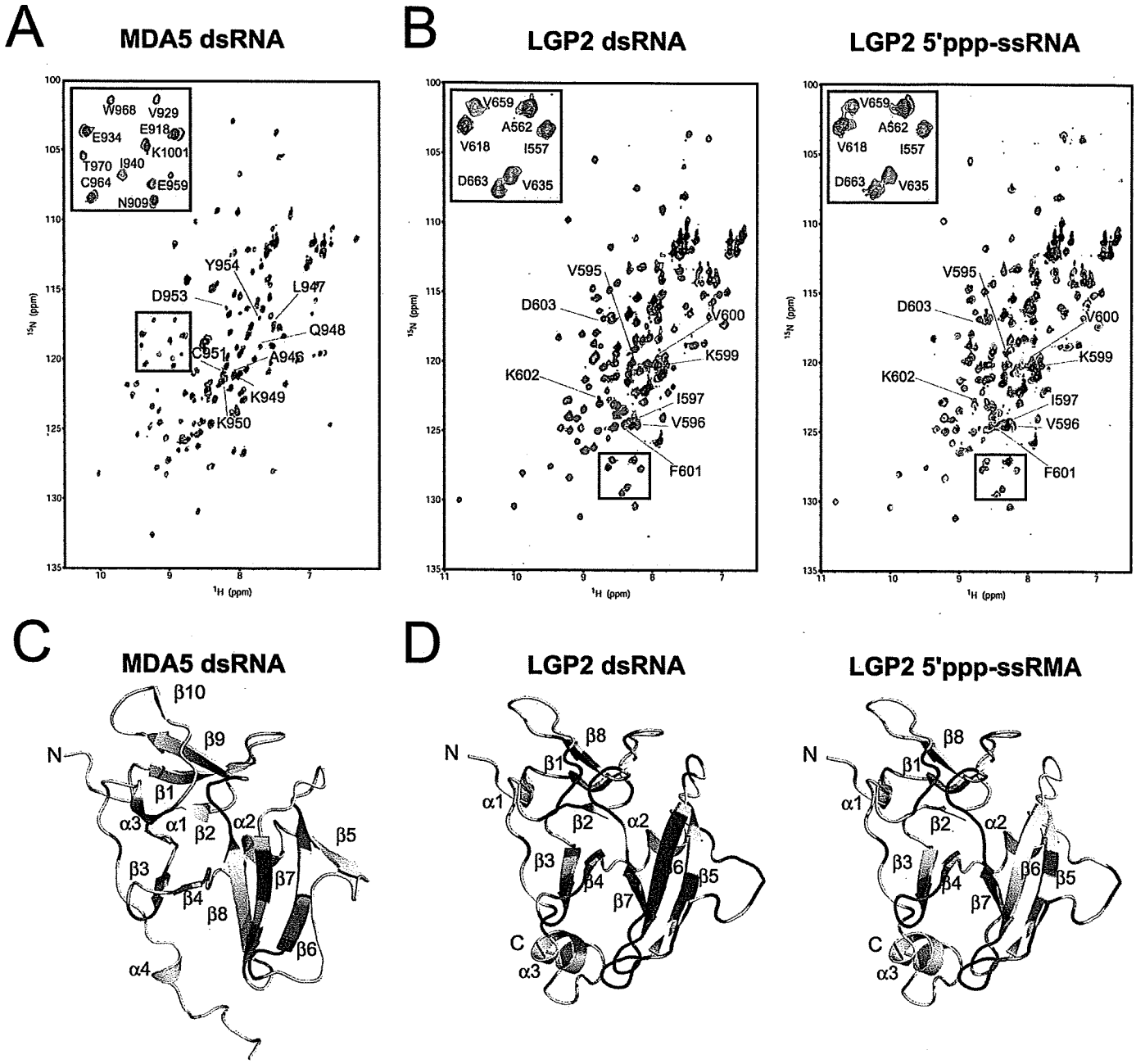

FIGURE 3. **NMR titration results for MDA5 CTD and LGP2 CTD.** *A*, NMR titration of MDA5 CTD with dsRNA. An overlay of ^{1}H-^{15}N HSQC spectra are shown in *red*, *yellow*, *green*, and *blue* at 0, 0.25, 0.5, and 1.0 equivalents (molar ratio of dsRNA to proteins), respectively, where the residues in the RNA binding loop are labeled. The *inset* shows the excerpt of the enclosed region of the spectrum with assignment. *B*, NMR titration of LGP2 CTD with dsRNA (*left panel*) and 5′ppp-ssRNA (*right panel*). The figures are prepared in the same manner as in *A*. *C*, mapping of the residues of MDA5 CTD affected by the addition of dsRNA on the *ribbon diagram*. The residues whose peaks disappeared on addition of 0.25 and 0.5 equivalent molar ratios of dsRNA to CTD are colored *blue* and *green*, respectively. *D*, mapping of the residues of LGP2 CTD affected by the addition of dsRNA and 5′ppp-ssRNA (*left* and *right panels*) on the *ribbon diagram*, colors are the same as in *C*. The orientations are the same as in Fig. 2, *A* and *B*.

EMSA—EMSA was performed essentially as described previously (8). The native gel was silver-stained (for unlabeled probe and protein), or subjected to radioactivity detection (for a ^{32}P-labeled probe). The 5′ppp-ssRNA was labeled by using 5′-^{32}P-pCp (PerkinElmer Life Sciences) and T4 RNA ligase (Takara, Ohtsu, Siga, Japan) following the manufacturer's instructions.

Preparation of dsRNA Docked with RIG-I and LGP2 CTDs—The crystal structure of RIG-I CTD (20) and short dsRNA derived from the crystal structure (PDB ID: 1YYW) were docked with the Molecular Docking Algorithm Patchdock (21). Ten residues from the basic surface of RIG-I CTD were applied as potential binding sites for RIG-I CTD, whereas no sites were applied for dsRNA. Then ten highest scoring structures were checked to establish whether they satisfy the NMR titration data. 6 of the 10 structures satisfied the NMR data, and orientations of dsRNA in those structures were similar. A dsRNA-docked model with LGP2 CTD was similarly calculated and 5 of 10 structures showed similar orientations of the dsRNA.

Solution Structures of MDA5 CTD and LGP2 CTD

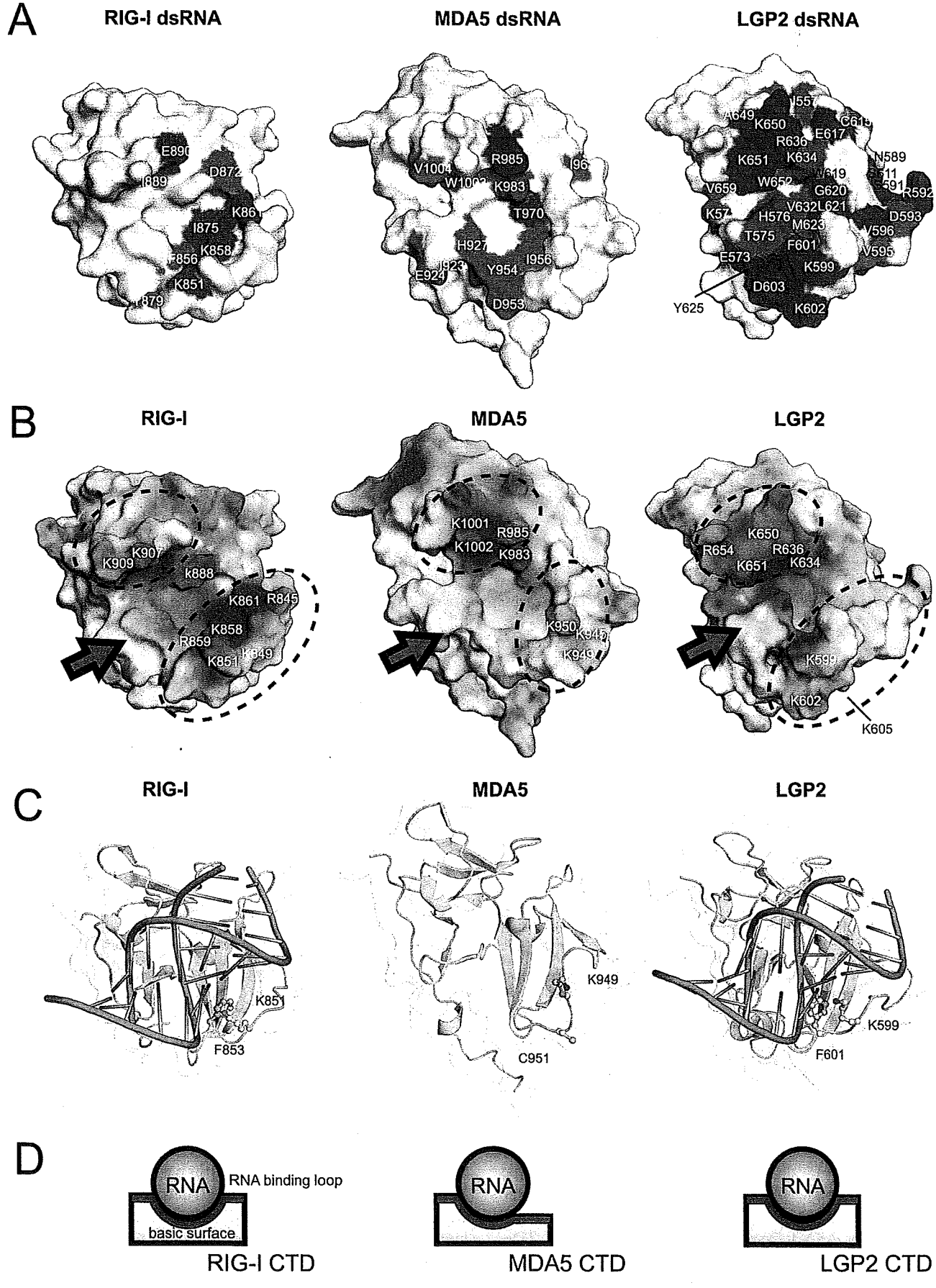

RESULTS

Characterization of RLR CTDs for Specific Binding to RNAs by SPR and EMSA—To investigate the RNA binding specificity of LGP2 CTD (546–678) and MDA5 CTD (896–1025), both CTDs were expressed as GST fusion proteins and were applied to the SPR analysis together with RIG-I CTD (792–925) (Fig. 1*B* and supplemental Fig. 1). The GST fusion proteins were captured on the sensor chip, and their affinities to 5′ppp-ssRNA, dsRNA, and the two complementary ssRNAs were tested. In the SPR experiment, RIG-I CTD was bound to dsRNA and 5′ppp-ssRNA specifically, but was not bound to the two ssRNAs as has also previously been observed by EMSA (8). The LGP2 CTD was strongly bound to dsRNA and 5′ppp-ssRNA, but it exhibited lower binding affinity to ssRNA. The MDA5 CTD did not bind to any of the RNAs tested under these conditions.

The RIG-I CTD has been reported to specifically bind to both dsRNA and 5′ppp-ssRNA by EMSA (8). We produced CTDs without the GST tag and compared the RNA-binding activity by EMSA (Fig. 1*C*). The CTD of RIG-I and LGP2 specifically bound to dsRNA and 5′ppp-ssRNA, but not to ssRNAs (data not shown). This result is consistent with that of the SPR analysis. The EMSA data shows the appearance of slower mobility complexes, most clearly observed with LGP2 CTD and dsRNA. These complexes are likely corresponding to dsRNA bound to multiple CTD molecules (see "Discussion"). The MDA5 CTD exhibited low binding affinity to dsRNA, and its biding affinity to 5′ppp-ssRNA was very low. This is reminiscent of the previous observation that full-length MDA5 bound much more weakly to poly(I:C)-Sepharose than to RIG-I (22) (supplemental Fig. 3). Summarizing, these results suggest that RLR CTDs play a critical role in the RNA recognition by RLR.

Solution Structures of MDA5 and LGP2 CTDs—The solution structures of MDA5 and LGP2 CTDs were determined by NMR (Fig. 2, *A* and *B*), and both MDA5 and LGP2 CTDs have a fold similar to that of RIG-I CTD and contain a single conserved Zn^{2+} binding site (Fig. 2, *C* and *D*). We confirmed that both CTDs contain a single Zn^{2+} ion, by atomic absorption spectroscopy, similar to RIG-I CTD (supplemental Table 1). The core of the structure is composed of a central anti-parallel β sheet (Fig. 2, *C* and *D*) (β3–β8 in RIG-I and MDA5, β3–β7 in LGP2). A further anti-parallel β sheet (β1, -2, and -9 in RIG-I; β1, -2, -9, and -10 in MDA5; β1, -2, and -8 in LGP2) is located on top of the central β sheet, and there are several short helices (α1–3 in RIG-I and MDA5, α1 and -2 in LGP2) attached to the two β sheets that help stabilize the structure of the CTDs. The C-terminal region of RIG-I, MDA5, and LGP2 CTDs has a long loop that is surrounding one edge of the central β sheet and the C-terminal helix (α4 in RIG-I and MDA5, α3 in LGP2) is located at the bottom of the central β sheet. The long loop between β5 and β6 that was implicated in RNA recognition in RIG-I, is also present in all RLR CTDs (termed "RNA Binding Loop" below). Recently, the crystal structure of LGP2 CTD was reported. Although the RNA binding loop was not observed in the crystal structure, the author implied that the loop is important for RNA specificity (23).

Although the RLR CTDs have a similar global fold with a large basic surface on the central β-sheet (see Fig. 4*B*), a close inspection of the RLR CTD structures shows small but appreciable differences (Fig. 2*C*). Similar to RIG-I, the C-terminal helices of LGP2 and MDA5 are located at the bottom of the central β-sheet and interacts with the loop between β6 and β7 (β7 and β8 in MDA5), whereas the C-terminal helix of MDA5 is projected outward. However, the regions following the C-terminal helix are flexible, because these regions exhibit small steady-state NOEs (<0.3 in supplemental Fig. 2). There is also an appreciable difference in the RNA binding loop. The N-terminal part of the RNA binding loop in MDA5 CTD is clipped onto the surface of β6 so that the conformation of the rest of the RNA binding loop is restricted and gives rise to an open and flat conformation (Fig. 2, *A* and *C*, *middle*). Thus, the basic surface becomes a more open structure (Figs. 2*C*, 4*B*, and 4*D* (*middle*)). Although the C-terminal RNA binding loop in LGP2 is restrained but stands upright on β6 and encloses the central β-sheet together with the central part of the loop between β8 and α3, a loop N terminus to β8, forming a basic groove (Figs. 2*C*, *right*, and 4*B*, *right*). A similar basic groove was identified as the RNA binding surface in RIG-I (Figs. 2*C* and 4*B*, *left*). Both RIG-I and LGP2 but not MDA5 share the common structural feature for the RNA binding loop. It is to be noted that the RNA binding loops in MDA5 and LGP2 are relatively restricted, based on the steady-state NOE measurements (>0.5 in supplemental Fig. 2).

NMR Titration of MDA5 and LGP2 CTDs—To establish whether the basic surfaces of MDA5 and LGP2 CTDs are responsible for the binding to viral RNAs, we performed NMR titration with the RNAs (dsRNA, 5′ppp-ssRNA, and ssRNAs), used in the SPR and EMSA assays reported above, against ^{15}N-labeled MDA5 and LGP2 CTDs (Fig. 3, *A* and *B*).

In MDA5 CTD, there were negligibly small chemical shift changes in the ^{1}H-^{15}N HSQC spectra even with addition of 2.0 equivalent molar ratios of 5′ppp-ssRNA and two ssRNAs, indicating an absence of interaction between MDA5 CTD and these RNAs (data not shown). However, upon addition of 0.5 equivalent molar ratio of dsRNA, an appreciable number of peaks disappeared possibly due to intermediate exchange processes (Fig. 3, *A* and *C*). The disappeared peaks were assigned to the residues on β3, β4 and their connecting loop, β6, β7, the loop C terminus to β8, and α3. However, most of the residues on the RNA binding loop other than Asp-953 and Tyr-954 did not

FIGURE 4. **Structural comparisons of RLR CTDs.** *A*, surface representation of the dsRNA affected surface of RLR CTDs (*left* to *right*, RIG-I CTD, MDA5 CTD, and LGP2 CTD). The residues that disappeared in NMR titration experiments upon addition of 0.25 and 0.5 equivalents of dsRNA are colored in *blue* and *green*, respectively. The residue numbers are also shown. The data of the dsRNA affected surface of RIG-I CTD was derived from our previous study (8). *B*, electrostatic surface potentials of the RLR CTDs (*left* to *right*, RIG-I CTD, MDA5 CTD, and LGP2 CTD). *Dotted circles* indicate the banks surrounding the basic surface. *C*, *left*, dsRNA-bound model of RIG-I CTD. *Right*, dsRNA-bound model of LGP2 CTD. The Lys and Phe residues in the RNA binding loop conserved in RIG-I and LGP2 are shown in *ball-and-stick models* and labeled. *Middle*, structure of MDA5 CTD, the residues corresponding to the Lys-851 and Phe-853 in RIG-I are shown. All figures are shown in the same structural orientation as in Fig. 2*A*. *D*, schematic diagrams of dsRNA bound to the basic surface of RIG-I CTD (*left*), MDA5 CTD (*mid*), and LGP2 CTD (*right*) viewed from the *arrows* indicated in Fig. 4*B*.

disappear (Fig. 3*C*). This strongly suggests that the MDA5 CTD uses the basic surface to interact with dsRNA similar to RIG-I, but the RNA binding loop does not appear to be involved in RNA binding. This result is consistent with EMSA (Fig. 1*C*) but not with the SPR analysis (Fig. 1*B*), where there was no interaction between MDA5 and dsRNA. This inconsistency may be due to the higher concentration of MDA5 CTD and dsRNA used in the EMSA and NMR titration studies than in the SPR studies.

For LGP2, even with addition of 2.0 equivalent molar ratios of ssRNAs, ^{1}H-^{15}N HSQC of LGP2 CTD spectra showed neither chemical shift changes nor any loss of signal intensities (data not shown), indicating that LGP2 CTD does not recognize ssRNAs. However, the addition of a 0.25 equivalent molar ratio of dsRNA and 0.5 equivalent molar ratio of 5′ppp-ssRNA caused the disappearance of a large number of peaks (Fig. 3*B*). When the residues corresponding to the peaks, which disappeared by dsRNA titration, were mapped on the three-dimensional structure of LGP2 CTD, these were located on β3, β4 and the connecting loop, the RNA binding loop, β5, β6 and the loop C terminus to β6, β7 and the loop between β7 and β8, and the C terminus to β8 (α3 in RIG-I) (Fig. 3*D*, *left*). The binding surface for 5′ppp-ssRNA is similar to that of dsRNA but is less extensive (Fig. 3*D*, *right*). It is to be noted that unlike MDA5, a large number of the peaks assigned on the RNA binding loop (Fig. 3*B*) disappeared in both cases, indicating that the RNA binding loop plays a critical role in the recognition of RNA ligands in LPG2. Residues of CTD involved in the interaction with dsRNA along with surface charges are mapped for comparison among RLRs (8) (Fig. 4, see "Discussion").

Analysis of the Structure-Function Relationship of RLR by Mutagenesis—We generated MDA5 mutants considering the results of the chemical shift perturbation study and the electrostatic surface potential (Fig. 4, *A* and *B*, *middle*). The KR983/985AA and KK1001/1002AA mutants were expressed in MDA5$^{-/-}$ mouse embryo fibroblasts, and next the ability to mediate the virus-responsive reporter gene activation was examined. To stimulate MDA5, the cells were transfected with poly(I:C), a known chemical ligand for MDA5 (Fig. 5*A*). Irrespective of the absence of MDA5, vector-transfected cells exhibited reporter activation upon stimulus by poly(I:C), presumably due to the activation of RIG-I by short poly(I:C) present in this batch of poly(I:C) (300–3000 bp, data not shown). Expression of wt MDA5 strongly enhanced this response, suggesting this increase is mediated by ectopically expressed MDA5. However both of the mutants exhibited only slight activation. Comparable levels of wt and mutant MDA5 were expressed in these cells (Fig. 5*B*), suggesting that mutated basic amino acid residues perform critical functions.

The solution structures and chemical shift perturbation studies of RIG-I and LGP2 may highlight the presence of the RNA binding loop. Because the specificity of RIG-I and LGP2 CTDs to viral RNAs are similar, we focused on a Phe residue that are conserved in the RNA binding loop of RIG-I and LGP2 but is not conserved in MDA5. First, we produced and purified full-length wt RIG-I and mutants with F853A and F853C that mimic MDA5 (Fig. 2*D*) and KK888/907AA (8) in 293T cells (Fig. 6*A*). Comparable levels of wt and mutant proteins were

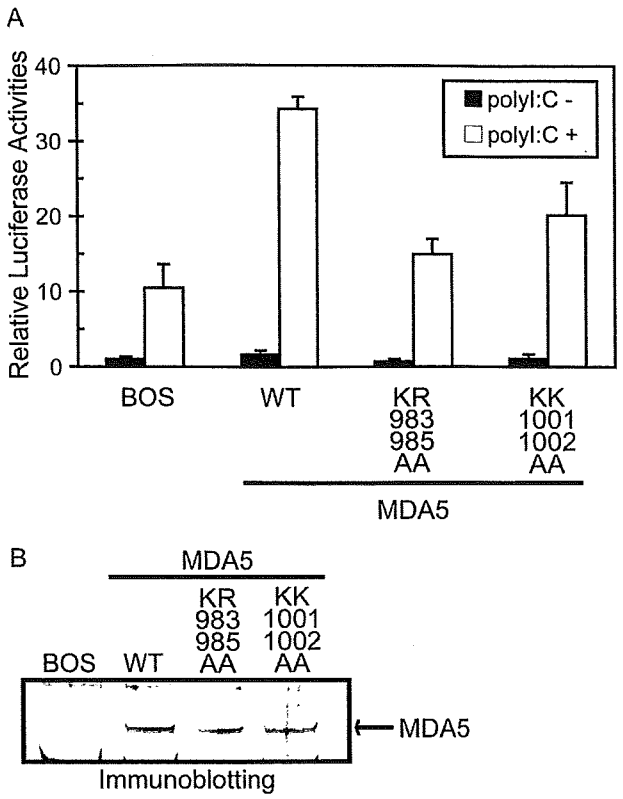

FIGURE 5. **Functional analysis of basic residue mutations of MDA5 on the basic surface.** *A*, MDA5$^{-/-}$ mouse embryo fibroblasts were transfected with the reporter gene, p-125Luc, and pRL-tk, together with the expression vector for MDA5 and mutants. Cells were stimulated by transfection with poly(I:C) and subjected to a dual-luciferase assay. The values are the means ± S.D. from triplicate experiments. The relative luciferase activity was calculated by considering the luciferase activity from cells transfected with empty vector (*BOS*) as 1.0. The cell lysates were analyzed for expression of MDA5 and mutants by Immunoblotting (*B*).

produced and recovered, suggesting that these mutations did not alter the stability of RIG-I (Fig. 6*A*). The purified proteins were subjected to EMSA using dsRNA and 5′ppp-RNA as probes (Fig. 6, *B* and *C*). The results clearly show that, along with the previously identified basic residues on the basic surface, Phe-853 in the RNA binding loop is critical for binding with dsRNA and 5′ppp-ssRNA. Further, the mutation of Phe-853 reduced the signaling activity of RIG-I when stimulated with these RNA species, particularly with dsRNA (Fig. 6, *D* and *E*). Next the involvement of the RNA binding loop in RNA recognition by LGP2 was examined. Three basic residues in the RNA binding loop or the conserved Phe were substituted (KKK599/602/605AAA, F601A, and F601C). These LGP2 mutant proteins along with the wt protein were produced and recovered at similar levels suggesting that these mutations did not affect protein stability dramatically (Fig. 7*A*). The purified LGP2 proteins were examined for RNA binding. The results in Fig. 7 (*B* and *C*) clearly show that the residues on the RNA binding loop are critical for LGP2 to recognize dsRNA and 5′ppp-ssRNA.

To directly compare RNA-binding activity of full-length RIG-I, MDA5, and LGP2 and their mutants, EMSA was performed under the same conditions (supplemental Fig. 3). The result shows that the binding properties of full-length RLRs are

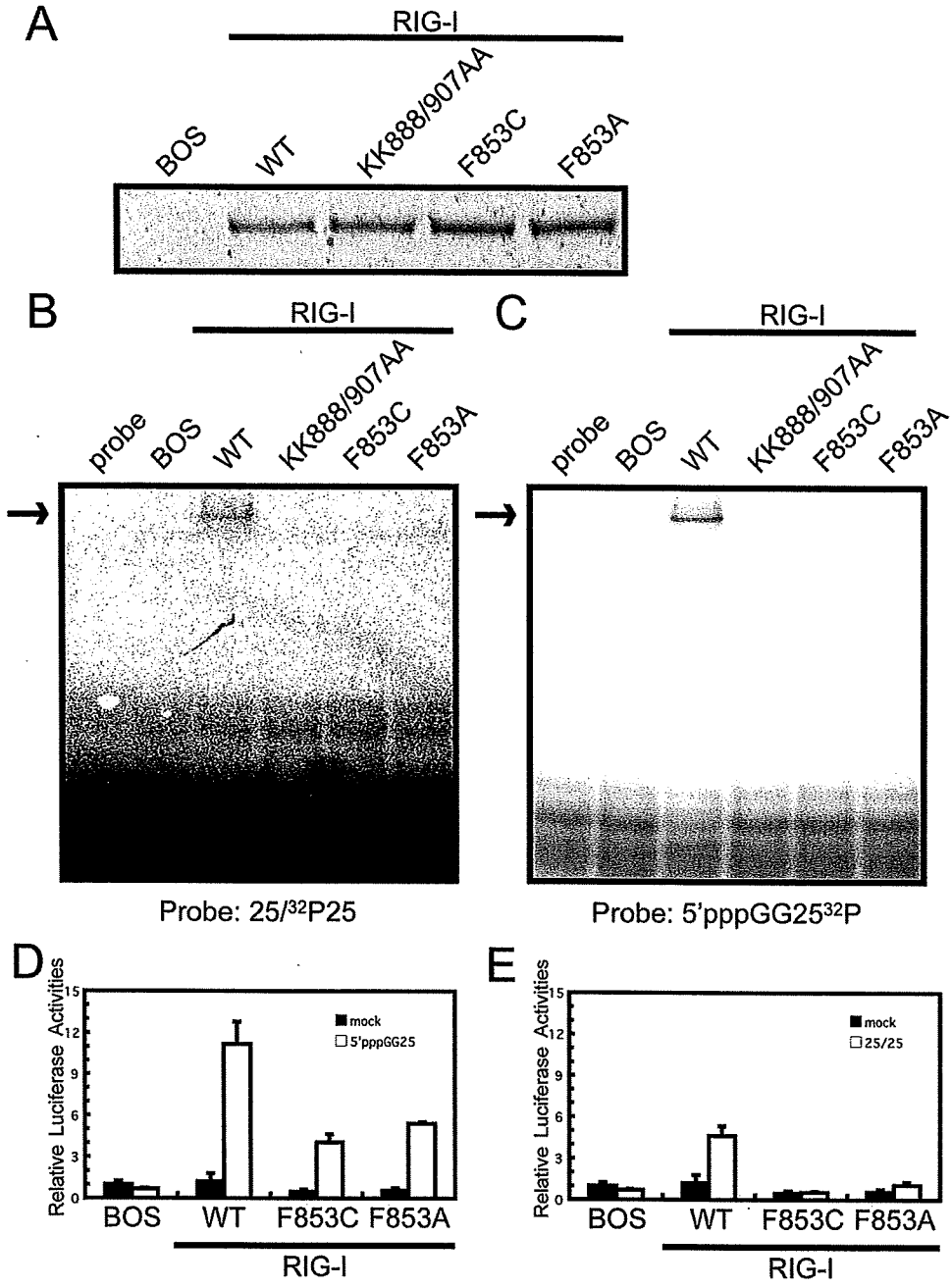

FIGURE 6. **Functional analysis of the basic surface and the RNA binding loop mutants of RIG-I.** Full-length wild type RIG-I and mutants were produced in 293T cells and purified by anti FLAG antibody. *A*, silver staining of the purified recombinant RIG-I. The recombinant RIG-I was subjected to EMSA using ^{32}P-labeled dsRNA (*B*; 25/25c) or 5'ppp-ssRNA (*C*; 5'pppGG25) as probe. *D* and *E*, interferon-β promoter activation by wt RIG-I and mutants. RIG-I$^{-/-}$ mouse embryo fibroblasts were transfected with the reporter gene, p-125Luc, and pRL-tk, together with the expression vector for RIG-I and mutants. Cells were stimulated by transfection with 25/25c (*D*) or 5'pppGG25 (*E*) and subjected to a dual-luciferase assay. The values are the means ± S.D. from triplicate experiments. The relative luciferase activity was calculated by considering the luciferase activity from cells transfected with empty vector (*BOS*) as 1.0.

closely reflecting those of CTD (Fig. 1*C*) and that mutations at critical residues prevented the RNA binding.

DISCUSSION

The experiments reported here compared the RNA-binding activity of CTDs of RLRs. The results of SPR and EMSA assays suggested that LGP2 CTD bound to dsRNA and 5'ppp-ssRNA with higher affinity than RIG-I, but that MDA5 CTD exhibited weaker binding.

The solution structure of the CTD revealed several critical features shared among or unique to each RLR. There is an RNA binding loop in all the CTDs, and the NMR structure and titration studies as well as the functional studies showed that the RNA binding loop in RIG-I and LGP2 are critical for RNA recognition but that it seems to be less important in MDA5. *In silico* docking with RIG-I (Fig. 4*C*) suggests that dsRNA lies on the basic groove of the RIG-I CTD, and that multiple interactions between the basic residues and phosphate backbone of the RNA maintains the complex. In the structure of the dsRNA-bound model of RIG-I CTD, the aromatic moiety of Phe-853 is stacked into the groove of the dsRNA via the hydrophobic interaction with a ribose moiety of the dsRNA. This interaction would anchor the position of both dsRNA and the RNA binding loop and allow the side chain of the conserved Lys-851 to form a stable electrostatic interaction with dsRNA. Whereas, in MDA5, the aromatic residue in this position is replaced by Cys, which would impair the hydrophobic interaction. Moreover, the flat surface formed by the RNA binding loop is not favorable for the binding between MDA5 and dsRNAs. On the other hand, the Phe-601 of LGP2 is located in a similar position and may similarly interact with the sugar moiety as is suggested in RIG-I (Fig. 4*C*). Taken together, both RIG-I CTD and LGP2 CTD bind to dsRNA and 5'ppp-ssRNA with high affinity. It is to be noted that slower migrating complexes are observed at higher protein concentrations, particularly with LGP2 (Fig. 1*C*). These complexes are likely multiple LGP2 molecules bound to single dsRNA molecules. Our model (Fig. 4*C*) allows binding of multiple CTDs with single dsRNA. Formation of RLR multimers on dsRNA or 5'ppp-ssRNA may facilitate signaling through CARD oligomerization (14).

Further, despite a low binding affinity, MDA5 CTD also recognizes dsRNA, and the residues present in the basic surface are critical for the signaling activity of MDA5 (Figs. 4 and 5), suggesting that MDA5 CTD participates in dsRNA recognition. However it is also known that full-length MDA5 exhibits lower

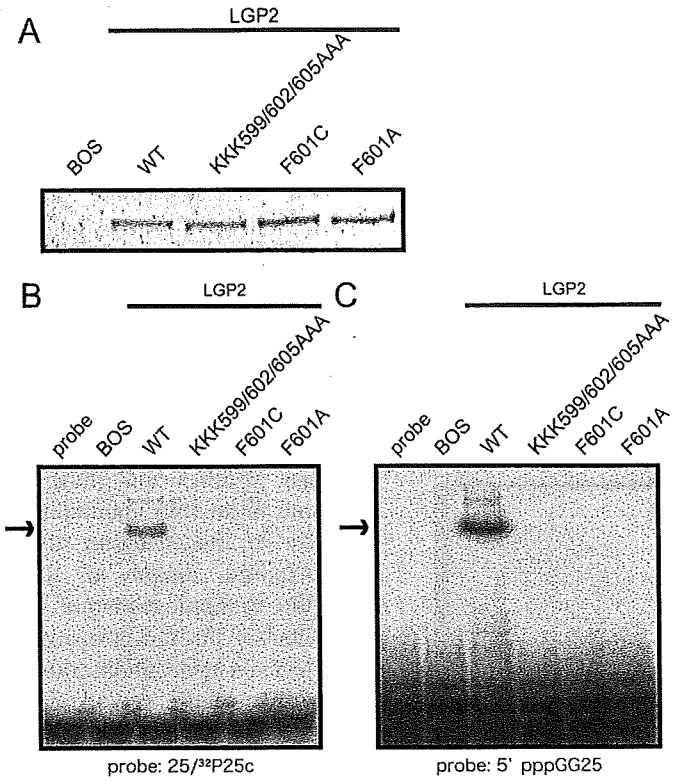

FIGURE 7. **Effect of the mutations of LGP2 on RNA recognition.** Full-length wild-type LGP2 and mutants on the RNA binding loop were produced in 293T cells and purified by anti FLAG antibody. *A*, silver staining of the purified recombinant LGP2. The recombinant LGP2 were subjected to EMSA using (*B*) ^{32}P-labeled dsRNA (25/25c) or (*C*) 5′ppp-ssRNA (C; 5′pppGG25) as probe. The *arrows* indicate the RNA-LGP2 complex.

binding affinity compared with LGP2 and RIG-I (22), suggesting that MDA5 may utilize some other RNA recognition protein. Related to this, LGP2$^{-/-}$ mice exhibit hypersensitivity to encephalomyocarditis virus (EMCV) infection (7), detection of which is mediated by MDA5 (5). Further, our preliminary result suggests that LGP2 and MDA5 bind to poly(I:C) in a cooperative manner (not shown).

Both RIG-I and LGP2 recognize dsRNA and 5′ppp-ssRNA, the two distinct non-self RNA patterns. In the case of 5′ppp-ssRNA recognition, 5′-end triphosphate is an apparent determinant of a non-self RNA. Although the model here provides a recognition mechanism of dsRNA by the CTD of RIG-I and LGP2, the recognition of 5′ppp-ssRNA by RIG-I and LGP2 need to be further substantiated. Interestingly, mutagenesis studies indicate that critical residues for dsRNA recognition are also indispensable for 5′ppp-ssRNA recognition (8) (Figs. 5–7), suggesting common structural features of these patterns. In summary, our functional and structural analyses have uncovered the mechanism underlying the different functions of each RLR molecule. During revision of the manuscript a report describing crystal structure of LGP2 CTD and dsRNA was published (24). The report essentially describes recognition of dsRNA ends by LGP2. However, the EMSA result shows that the end structure of dsRNA does not affect recognition by LGP2 (supplemental Fig. 4). Apparently, further analyses are required to elucidate the mechanism of dsRNA recognition by RLR.

REFERENCES

1. Akira, S., Uematsu, S., and Takeuchi, O. (2006) *Cell* **124,** 783–801
2. Yoneyama, M., Kikuchi, M., Natsukawa, T., Shinobu, N., Imaizumi, T., Miyagishi, M., Taira, K., Akira, S., and Fujita, T. (2004) *Nat. Immunol.* **5,** 730–737
3. Hornung, V., Ellegast, J., Kim, S., Brzózka, K., Jung, A., Kato, H., Poeck, H., Akira, S., Conzelmann, K. K., Schlee, M., Endres, S., and Hartmann, G. (2006) *Science* **314,** 994–997
4. Pichlmair, A., Schulz, O., Tan, C. P., Näslund, T. I., Liljeström, P., Weber, F., Reis, E., and Sousa, C. (2006) *Science* **314,** 997–1001
5. Kato, H., Takeuchi, O., Sato, S., Yoneyama, M., Yamamoto, M., Matsui, K., Uematsu, S., Jung, A., Kawai, T., Ishii, K. J., Yamaguchi, O., Otsu, K., Tsujimura, T., Koh, C. S., Reis e Sousa, C., Matsuura, Y., Fujita, T., and Akira, S. (2006) *Nature* **441,** 101–105
6. Loo, Y. M., Fornek, J., Crochet, N., Bajwa, G., Perwitasari, O., Martinez-Sobrido, L., Akira, S., Gill, M. A., García-Sastre, A., Katze, M. G., and Gale, M., Jr. (2008) *J. Virol.* **82,** 335–345
7. Venkataraman, T., Valdes, M., Elsby, R., Kakuta, S., Caceres, G., Saijo, S., Iwakura, Y., and Barber, G. N. (2007) *J. Immunol.* **178,** 6444–6455
8. Takahasi, K., Yoneyama, M., Nishihori, T., Hirai, R., Kumeta, H., Narita, R., Gale, M., Jr., Inagaki, F., and Fujita, T. (2008) *Mol. Cell* **29,** 428–440
9. Kawai, T., Takahashi, K., Sato, S., Coban, C., Kumar, H., Kato, H., Ishii, K. J., Takeuchi, O., and Akira, S. (2005) *Nat. Immunol.* **6,** 981–988
10. Meylan, E., Curran, J., Hofmann, K., Moradpour, D., Binder, M., Bartenschlager, R., and Tschopp, J. (2005) *Nature* **437,** 1167–1172
11. Seth, R. B., Sun, L., Ea, C. K., and Chen, Z. J. (2005) *Cell* **122,** 669–682
12. Xu, L. G., Wang, Y. Y., Han, K. J., Li, L. Y., Zhai, Z., and Shu, H. B. (2005) *Mol. Cell* **19,** 727–740
13. Saito, T., Hirai, R., Loo, Y. M., Owen, D., Johnson, C. L., Sinha, S. C., Akira, S., Fujita, T., and Gale, M., Jr. (2007) *Proc. Natl. Acad. Sci. U. S. A.* **104,** 582–587
14. Yoneyama, M., and Fujita, T. (2008) *Immunity* **29,** 178–181
15. Higuchi, R., Krummel, B., and Saiki, R. K. (1988) *Nucleic Acids Res.* **16,** 7351–7367
16. Delaglio, F., Grzesiek, S., Vuister, G. W., Zhu, G., Pfeifer, J., and Bax, A. (1995) *J. Biomol. NMR* **6,** 277–293
17. Cornilescu, G., Delaglio, F., and Bax, A. (1999) *J. Biomol. NMR* **13,** 289–302
18. Güntert, P., Mumenthaler, C., and Wüthrich, K. (1997) *J. Mol. Biol.* **273,** 283–298
19. Herrmann, T., Güntert, P., and Wüthrich, K. (2002) *J. Mol. Biol.* **319,** 209–227
20. Cui, S., Eisenächer, K., Kirchhofer, A., Brzózka, K., Lammens, A., Lammens, K., Fujita, T., Conzelmann, K. K., Krug, A., and Hopfner, K. P. (2008) *Mol. Cell* **29,** 169–179
21. Schneidman-Duhovny, D., Inbar, Y., Nussinov, R., and Wolfson, H. J. (2005) *Nucleic Acids Res.* **33,** W363–367, web server issue
22. Yoneyama, M., Kikuchi, M., Matsumoto, K., Imaizumi, T., Miyagishi, M., Taira, K., Foy, E., Loo, Y. M., Gale, M., Jr., Akira, S., Yonehara, S., Kato, A., and Fujita, T. (2005) *J. Immunol.* **175,** 2851–2858
23. Pippig, D. A., Hellmuth, J. C., Cui, S., Kirchhofer, A., Lammens, K., Lammens, A., Schmidt, A., Rothenfusser, S., and Hopfner, K. P. (2009) *Nucleic Acids Res.* **37,** 2014–2025
24. Li, X., Ranjith-Kumar, C. T., Brooks, M. T., Bharmaiah, S., Herr, A. B., Kao, C., and Li, P. (2009) *J. Biol. Chem.*

JOURNAL OF VIROLOGY, Mar. 2009, p. 2338–2348
0022-538X/09/$08.00+0 doi:10.1128/JVI.01840-08

Vol. 83, No. 5

Arsenic Trioxide Inhibits Hepatitis C Virus RNA Replication through Modulation of the Glutathione Redox System and Oxidative Stress[▽]

Misao Kuroki,[1] Yasuo Ariumi,[1] Masanori Ikeda,[1] Hiromichi Dansako,[1] Takaji Wakita,[2] and Nobuyuki Kato[1]*

Department of Tumor Virology, Okayama University Graduate School of Medicine, Dentistry, and Pharmaceutical Sciences, 2-5-1, Shikata-cho, Okayama 700-8558, Japan,[1] and Department of Virology II, National Institute of Infectious Diseases, 1-23-1 Toyama, Shinjuku-ku, Tokyo 162-8640, Japan[2]

Received 2 September 2008/Accepted 13 December 2008

Arsenic trioxide (ATO), a therapeutic reagent used for the treatment of acute promyelocytic leukemia, has recently been reported to increase human immunodeficiency virus type 1 infectivity. However, in this study, we have demonstrated that replication of genome-length hepatitis C virus (HCV) RNA (O strain of genotype 1b) was notably inhibited by ATO at submicromolar concentrations without cell toxicity. RNA replication of HCV-JFH1 (genotype 2a) and the release of core protein into the culture supernatants were also inhibited by ATO after the HCV infection. To clarify the mechanism of the anti-HCV activity of ATO, we examined whether or not PML is associated with this anti-HCV activity, since PML is known to be a target of ATO. Interestingly, we observed the cytoplasmic translocation of PML after treatment with ATO. However, ATO still inhibited the HCV RNA replication even in the PML knockdown cells, suggesting that PML is dispensable for the anti-HCV activity of ATO. In contrast, we found that *N*-acetyl-cysteine, an antioxidant and glutathione precursor, completely and partially eliminated the anti-HCV activity of ATO after 24 h and 72 h of treatment, respectively. In this context, it is worth noting that we found an elevation of intracellular superoxide anion radical, but not hydrogen peroxide, and the depletion of intracellular glutathione in the ATO-treated cells. Taken together, these findings suggest that ATO inhibits the HCV RNA replication through modulation of the glutathione redox system and oxidative stress.

Hepatitis C virus (HCV) is the causative agent of chronic hepatitis, which progresses to liver cirrhosis and hepatocellular carcinoma. HCV is an enveloped virus with a positive single-stranded 9.6-kb RNA genome, which encodes a large polyprotein precursor of approximately 3,000 amino acid residues. This polyprotein is cleaved by a combination of the host and viral proteases into at least 10 proteins in the following order: core, envelope 1 (E1), E2, p7, nonstructural 2 (NS2), NS3, NS4A, NS4B, NS5A, and NS5B (30).

Alpha interferon has been used as an effective anti-HCV reagent in clinical therapy for patients with chronic hepatitis C. The current combination treatment with pegylated alpha interferon and ribavirin, a nucleoside analogue, has been shown to improve the sustained virological response rate to more than 50% (15). However, the adverse effects of the combination therapy and the limited efficacy against genotype 1b warrant the development of new anti-HCV reagents.

Arsenic trioxide (ATO) (As_2O_3, arsenite) has been used as a therapeutic reagent in acute promyelocytic leukemia, which bears an oncogenic PML-retinoic acid receptor alpha fusion protein resulting from chromosomal translocation (51, 52, 68, 70). The ATO treatment induces complete remission through degradation of the aberrant PML-retinoic acid receptor α (70). The PML tumor suppressor protein is required for formation of the PML nuclear body (PML-NB), also known as nuclear dot 10 or the PML oncogenic domain, which is often disrupted by infection with DNA viruses, such as herpes simplex virus type 1, human cytomegalovirus, and Epstein-Barr virus (17). The treatment with ATO results in degradation of the PML protein and disruption of the PML-NB (70). Therefore, ATO has been become a useful probe for investigating the functions of the PML-NB, including cell growth, apoptosis, stress response, and viral infection. Indeed, ATO has been shown to increase retroviral infectivity, such as human immunodeficiency virus type 1 (HIV-1) and murine leukemia virus infectivity, but the mechanisms of this change are not well understood (5, 6, 32, 44, 47, 50, 57). In contrast, ATO was recently reported to inhibit the replication of HCV subgenomic replicon RNA (24). However, it also remains unclear how ATO inhibits the HCV RNA replication. In this study, using genome-length HCV RNA replication systems, we investigated the molecular mechanism(s) of the anti-HCV activity of ATO, and we provide evidence that ATO inhibits HCV RNA replication through modulation of the glutathione redox system and oxidative stress.

MATERIALS AND METHODS

Reagents. ATO, *N*-acetyl-cysteine (NAC), ascorbic acid (vitamin C), and L-buthionine sulfoximine (BSO) were purchased from Sigma (St. Louis, MO). Arsenic pentoxide (APO) (As_2O_5, arsenate) was purchased from Wako (Osaka, Japan). Both ATO and APO were dissolved in 1 N NaOH at 0.1 M as a stock solution. An inducible nitric oxide synthase (iNOS) inhibitor, 1400W, was purchased from Calbiochem (Merck Biosciences, Darmstadt, Germany).

Cell culture. 293FT cells were cultured in Dulbecco's modified Eagle's medium (Invitrogen, Carlsbad, CA, USA) supplemented with 10% fetal bovine serum. The following four HuH-7-derived cell lines or their parental HuH-7 cells

* Corresponding author. Mailing address: Department of Tumor Virology, Okayama University Graduate School of Medicine, Dentistry, and Pharmaceutical Sciences, 2-5-1, Shikata-cho, Okayama 700-8558, Japan. Phone: 81 86 235 7385. Fax: 81 86 235 7392. E-mail: nkato@md.okayama-u.ac.jp.

▽ Published ahead of print on 24 December 2008.

were cultured in Dulbecco's modified Eagle's medium with 10% fetal bovine serum as described previously (25): O cells, harboring a replicative genome-length HCV-O RNA (O strain of genotype 1b) (25); OR6 cells, harboring the genome-length HCV-O RNA with luciferase as a reporter (25); sO cells, harboring the subgenomic replicon RNA of HCV-O (31); and RSc cured cells, which cell culture-generated HCV-JFH1 (JFH1 strain of genotype 2a) (58) could infect and effectively replicate in (2, 3). The O, OR6, and sO cells were maintained in the presence of G418 (300 μg/ml Geneticin; Invitrogen).

RNA interference. Oligonucleotides with the following sense and antisense sequences were used for the cloning of short hairpin RNA (shRNA)-encoding sequences targeted to PML (56) in a lentiviral vector: 5′-GATCCCCAGATGC AGCTGTATCCAAGTTCAAGAGACTTGGATACAGCTGCATCTTTTTTG GAAA-3′ (sense) and 5′-AGCTTTTCCAAAAAAGATGCAGCTGTATCCAA GTCTCTTGAACTTGGATACAGCTGCATCTGGG-3′ (antisense). , These oligonucleotides were annealed and subcloned into the BglII-HindIII site, downstream from an RNA polymerase III promoter of pSUPER (8), to generate pSUPER-PMLi. To construct pLV-PMLi, the BamHI-SalI fragments of pSUPER-PMLi were subcloned into the BamHI-SalI site of pRDI292, an HIV-1-derived self-inactivating lentiviral vector containing a puromycin resistance marker allowing for the selection of transduced cells (7). pLV-Chk2i was described previously (3).

Lentiviral vector production. The vesicular stomatitis virus (VSV) G-pseudotyped HIV-1-based vector system has been described previously (42). The lentiviral vector particles were produced by transient transfection of the second-generation packaging construct pCMV-ΔR8.91 (1, 71) and the VSV G envelope-expressing plasmid pMDG2 as well as pRDI292 into 293FT cells with FuGene6 (Roche Diagnostics, Mannheim, Germany).

HCV infection experiments. The supernatants was collected from cell culture-generated HCV-JFH1 (58)-infected RSc cells (2, 3) at 5 days postinfection and stored at −80°C after filtering through a 0.45-μm filter (Kurabo, Osaka, Japan) until use. For infection experiments with HCV-JFH1 virus, RSc cells (1×10^5 cells/well) were plated onto six-well plates and cultured for 24 h. We then infected the cells with 50 μl (equivalent to a multiplicity of infection of 0.05 to 0.1) of inoculum. The culture supernatants were collected at 97 h postinfection, and the levels of the core protein were determined by enzyme-linked immunosorbent assay (Mitsubishi Kagaku Bio-Clinical Laboratories, Tokyo, Japan). Total RNA was isolated from the infected cellular lysates using an RNeasy minikit (Qiagen, Hilden, Germany) for quantitative reverse transcription-PCR (RT-PCR) analysis of intracellular HCV RNA. The level of intracellular HCV RNA in the RSc cells was $>10^8$ copies/μg total RNA at 4 days postinfection.

Quantitative RT-PCR Analysis. The quantitative RT-PCR analysis for HCV RNA was performed by real-time LightCycler PCR (Roche) as described previously (25). We used the following forward and reverse primer sets for the real-time LightCycler PCR: PML, 5′-GAGGAGTTCCAGTTTCTGCG-3′ (forward), 5′-GCGCCTGGCAGATGGGGCAC-3′ (reverse); β-actin, 5′-TGACGG GGTCACCCACACTG-3′ (forward), 5′-AAGCTGTAGCCGCGCTCGGT-3′ (reverse); HCV-O, 5′-AGAGCCATAGTGGTCTGCGG-3′ (forward), 5′-CTT TCGCGACCCAACACTAC-3′ (reverse); and HCV-JFH1, 5′-5′-AGAGCCAT AGTGGTCTGCGG-3′ (forward), 5′-CTTTCGCAACCCAACGCTAC-3′ (reverse).

Western blot analysis. Cells were lysed in buffer containing 50 mM Tris-HCl (pH 8.0), 150 mM NaCl, 4 mM EDTA, 1% Nonidet P-40, 0.1% sodium dodecyl sulfate, 1 mM dithiothreitol, and 1 mM phenylmethylsulfonyl fluoride. Supernatants from these lysates were subjected to sodium dodecyl sulfate-polyacrylamide gel electrophoresis, followed by immunoblot analysis using anti-PML (A301-168A-1; Bethyl Laboratories, Montgomery, TX), anti-Chk2 (DCS-273; Medical & Biological Laboratories, MBL, Nagoya, Japan), anti-HCV core (CP-9 and CP-11; Institute of Immunology, Tokyo, Japan), anti-HCV NS5A (no. 8926; a generous gift from A Takamizawa, The Research Foundation for Microbial Diseases of Osaka University, Japan), anti-signal transducer and activator of transcription 3 (anti-STAT3) (BD Bioscience, San Jose, CA), anti-phospho-STAT3 (Tyr705) (Cell Signaling Technology, Danvers, MA) anti-poly(ADP-ribose) polymerase 1 (anti-PARP-1) (C-2-10; Calbiochem), or anti-β-actin antibody (Sigma).

MTT assay. HuH-7 or O cells (5×10^3 cells/well) were plated onto 96-well plates and cultured for 24 h. The cells were treated with ATO, APO, or NaOH for 24, 48, or 72 h and then subjected to the colorimetric 3-(4,5-dimethylthiazol-2-yl)-2,5-diphenyltetrazolium bromide (MTT) assay according to the manufacturer's instructions (cell proliferation kit I; Roche). The absorbance was read using a microplate reader (model 2550; Bio-Rad Laboratories, Hercules, CA) at 550 nm with a reference wavelength of 690 nm.

RL assay. OR6 cells (1.5×10^4 cells/well) were plated onto 24-well plates and cultured for 24 h. The cells were treated with each reagent for 72 h and then subjected to the *Renilla* luciferase (RL) assay according to the manufacturer's instructions (Promega, Madison, WI). A Lumat LB9507 luminometer (Berthold, Bad Wildbad, Germany) was used to detect RL activity.

FL assay. Plasmids were transfected into O cells (2×10^4 cells/well in 24-well plates) using FuGene6 and cultured for 24 h. The cells were treated with or without 1 μM ATO for 24 h, and then firefly luciferase (FL) assays were performed according to the manufacturer's instructions (Promega).

Immunofluorescence and confocal microscopic analysis. Cells were fixed in 3.6% formaldehyde in phosphate-buffered saline (PBS), permeabilized in 0.1% NP-40 in PBS at room temperature, and incubated with anti-PML antibody (PM001; MBL) at a 1:300 dilution in PBS containing 3% bovine serum albumin at 37°C for 30 min. They were then stained with fluorescein isothiocyanate-conjugated anti-rabbit antibody (Jackson ImmunoResearch, West Grove, PA) at a 1:300 dilution in PBS containing bovine serum albumin at 37°C for 30 min, followed by staining with 4′,6-diamidino-2-phenylindole (DAPI) at room temperature for 15 min. Following extensive washing in PBS, the cells were mounted on slides using a mounting medium of 90% glycerin–10% PBS with 0.01% *p*-phenylenediamine added to reduce fading. Samples were viewed under a confocal laser-scanning microscope (LSM510; Zeiss, Jena, Germany).

Measurement of intracellular O_2^- and H_2O_2 production. The intracellular superoxide anion radical (O_2^-) levels were measured with an oxidation-sensitive fluorescent probe, dihydroethidium (DHE) (Invitrogen Molecular Probes), that is highly selective for detection of O_2^- among reactive oxygen species (ROS). DHE is cell permeative and reacts with O_2^- to form ethidium, which in turn intercalates in DNA, thereby exhibiting a red fluorescence. The intracellular hydrogen peroxide (H_2O_2) levels were measured with another oxidation-sensitive fluorescent probe dye, 6-carboxy-2′,7′-dichlorodihydrofluorescein diacetate (carboxy-H_2DCFDA) (Invitrogen Molecular Probes). Carboxy-H_2DCFDA was intracellularly deacetylated with esterase and further oxidized with peroxidase to the fluorescent 2′,7′-dichlorodihydrofluorescein (DCF). The ATO- or BSO-treated O cells were washed with PBS and incubated with 5 μM DHE and 20 μM carboxy-H_2DCFDA in PBS at 37°C for 30 min. Cells were then washed twice with PBS. The DHE or DCF fluorescence intensity was measured using a FACSCalibur flow cytometer. For each sample, 10,000 events were collected. The O_2^- or H_2O_2 levels are indicated as mean fluorescence intensities, which were determined with the CellQuest software (BD Bioscience).

Detection of intracellular glutathione. Intracellular glutathione levels were analyzed using CellTracker Green (5-chloromethylfluorescein diacetate [CMFDA]; Molecular Probes, Invitrogen). CMFDA is a membrane-permeative dye used to determine intracellular glutathione levels. Cytoplasmic esterase converts the nonfluorescent CMFDA to the fluorescent 5-chloromethylfluorescein (CMF), which can then react with glutathione. The excitation peak is at 492 nm, and the fluorescence emission peak is at 517 nm. O cells treated with 1 μM ATO for 72 h were washed with PBS and incubated with 5 μM CMFDA at 37°C for 30 min. The CMF fluorescence intensity was measured using a FACSCalibur flow cytometer. For each sample, 10,000 events were collected. The glutathione levels are given as the relative mean fluorescence intensities, which were determined with CellQuest software.

RESULTS

ATO inhibits HCV RNA replication. First, we quantitatively examined the effect of ATO on the HCV RNA replication in HuH-7-derived O cells harboring a replicative genome-length HCV-O RNA (25). We found that submicromolar concentrations of ATO markedly inhibited genome-length HCV-O RNA replication in the O cells at 72 h after administration (Fig. 1A). The 50% effective concentration (EC_{50}) of ATO required for inhibition of genome-length HCV-O RNA replication was 0.19 μM (Fig. 1A). Consistent with this finding, the expression levels of the HCV core and NS5A proteins were also significantly decreased in the cell lysates of O cells treated with ATO for 72 h (Fig. 1B). In addition, ATO markedly inhibited the replication of the subgenomic replicon RNA (31), with an EC_{50} of 0.48 μM at 72 h after the treatment (Fig. 1C). We next examined the effect of ATO on HCV reproduction by HCV-JFH1 infection (58). The results revealed that ATO significantly inhibited the intracellular RNA replication of HCV-

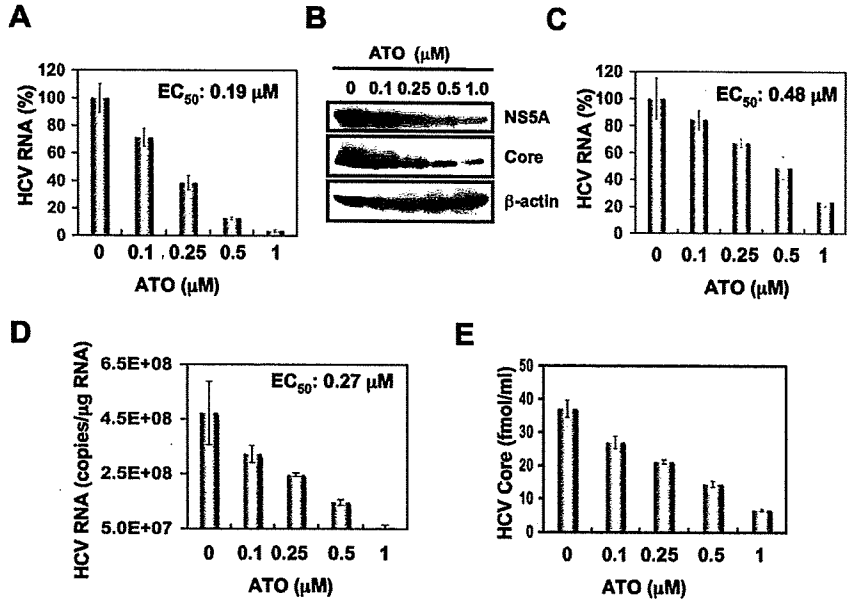

FIG. 1. Inhibition of HCV RNA replication by ATO. (A) The level of genome-length HCV RNA in O cells after the treatment with ATO was monitored by real-time LightCycler PCR. Experiments were done in triplicate and, bars represent the mean percentage of HCV RNA. Error bars indicate standard deviations. (B) HCV core and NS5A protein expression levels in O cells after treatment with ATO. The results of Western blot analysis of cellular lysates with anti-HCV core, anti-HCV NS5A, or anti-β-actin antibody in O cells at 72 h after treatment with ATO at the indicated concentration are shown. (C) The level of subgenomic replicon RNA was monitored by real-time LightCycler PCR. Results from three independent experiments conducted as described for panel A are shown. (D) The level of intracellular genome-length HCV-JFH1 RNA was monitored by real-time LightCycler PCR. RSc cells were pretreated with the indicated concentration of ATO for 13 h, followed by inoculation of the HCV-JFH1 virus, and then the infected cells were further incubated with ATO for 97 h. Results from three independent experiments conducted as described for panel A are shown. (E) The levels of the core protein in the culture supernatants treated as described for panel D were determined by enzyme-linked immunosorbent assay. Experiments were done in triplicate, and bars represent the mean core protein levels.

JFH1, with an EC_{50} of 0.27 μM, as well as the release of core protein into the culture supernatants in HuH-7-derived RSc cells at 97 h after inoculation of the HCV-JFH1 virus (Fig. 1D and E). Thus, we have demonstrated for the first time that ATO can inhibit the reproduction of HCV and particularly HCV RNA replication.

Effect of APO on HCV replication. Arsenic is known to exist in two oxidation states, As(III) in ATO and As(V) in APO. As ATO in the lower valence state has been reported to be more toxic than APO (48), we compared their anti-HCV activities using an OR6 assay system, which was recently developed as a luciferase reporter assay system for monitoring genome-length HCV RNA replication in HuH-7-derived OR6 cells (Fig. 2A) (25). The results showed that APO could not strongly suppress HCV replication at submicromolar concentrations, while ATO strongly inhibited it, with an EC_{50} of 0.33 μM (Fig. 2B and C), indicating that ATO has unique anti-HCV activity. In this context, it is relevant that the expression level of HCV core protein was also remarkably decreased in the cell lysates of O cells treated with ATO, but not those treated with APO, for 72 h (Fig. 2D). Thus, APO seems to be a useful negative probe to clarify the mechanism of the anti-HCV activity of ATO.

ATO does not affect cell growth at submicromolar concentrations. ATO has been reported to induce apoptosis (11, 14, 20, 21, 26–28, 33, 48, 66). Therefore, such an ATO-induced apoptosis may be involved in the anti-HCV activity. To test this possibility, we examined the effect of ATO or APO at various concentrations on cell proliferation by colorimetric MTT assay. In this context, we demonstrated that ATO did not affect the cell proliferation of O cells or the parental HCV-negative HuH-7 cells at submicromolar concentrations (Fig. 3A and E). In contrast, 4 or 8 μM ATO significantly inhibited cell proliferation (Fig. 3B and F). Similarly, APO did not affect the cell proliferation at less than 2 μM (Fig. 3C and D). Consistent with the above results, ATO-treated O cells exhibited normal growth rates and cell viabilities, at least at 1 μM for 72 h (Fig. 3G). Furthermore, we did not observe the cleavage of PARP-1, which is known to be an important substrate for activated caspase 3, in O cells treated with 1 μM ATO at least until 72 h (Fig. 3H), indicating that 1 μM ATO did not induce apoptosis in O cells. Thus, we concluded that the anti-HCV activity was independent of ATO-induced apoptosis or cell toxicity, at least at submicromolar concentrations.

PML and Chk2 are dispensable for the anti-HCV activity of ATO. Since PML is known to be a target of ATO (70), we first examined the subcellular localization of PML in O cells treated with either 1 μM ATO or 1 μM APO for 72 h by means of an anti-PML antibody (PM001; MBL) that can recognize most of the PML splicing variants and is useful for immunofluorescence analysis. The results showed that PML was localized predominantly in punctate nuclear speckles termed PML-NBs in control O cells (Fig. 4A). Interestingly, we noticed that some nuclear PML, but not all, disappeared and was translocated into discrete cytoplasmic bodies in the O cells treated with 1 μM ATO (Fig. 4A). We also observed cytoplasmic translocation of PML in the O cells treated with 1 μM APO for 72 h (Fig. 4A). Furthermore, we observed a similar cytoplasmic translocation of PML in the HCV-negative 293FT or HeLa

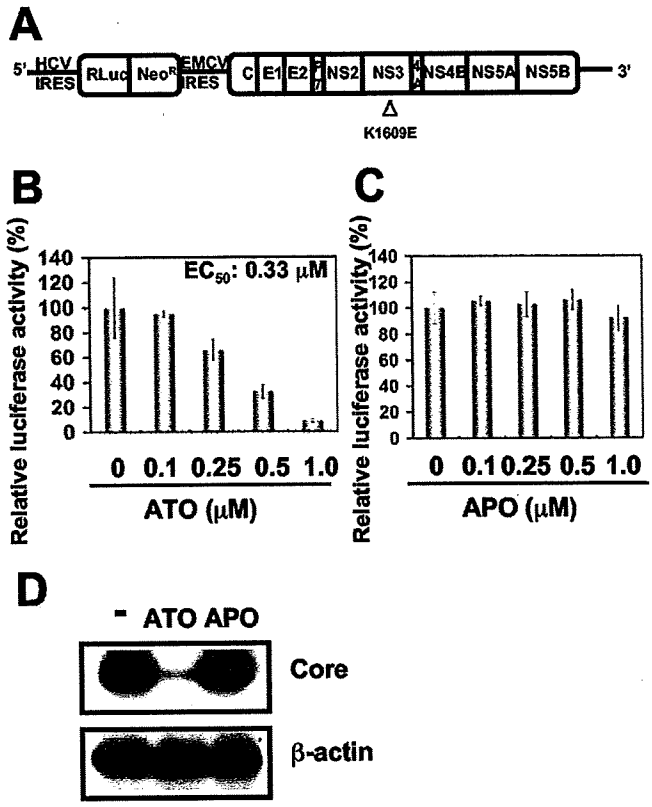

FIG. 2. Effect of APO on HCV replication. (A) Schematic representation of genome-length HCV RNA encoding the RL gene as a reporter (ORN/C-5B/KE RNA) replicated in OR6 cells. The RL is expressed as a fusion protein with neomycin phosphotransferase (Neo^R). The position of an adaptive mutation, K1609E in NS3, is indicated by an open triangle. (B) Effect of ATO on genome-length HCV RNA replication. At 72 h after treatment of OR6 cells with ATO at the indicated concentrations, the replication level of HCV RNA was monitored by the RL assay. The relative RL activity is shown. The results shown are means from three independent experiments. Error bars indicate standard deviations. (C) Effect of APO on genome-length HCV RNA replication. At 72 h after treatment of OR6 cells with APO at the indicated concentrations, the replication level of HCV RNA was monitored by the RL assay as described for panel B. (D) HCV core protein expression level in O cells after treatment with either ATO or APO. The results of Western blot analysis of cellular lysates with anti-HCV core or anti-β-actin antibody in O cells at 72 h after treatment with either 1 μM ATO or 1 μM APO are shown.

cells after the treatment with ATO (data not shown). Thus, we concluded that the cytoplasmic translocation of PML after the treatment with ATO was not associated with anti-HCV activity. Next, Western blot analysis to compare PML expression in the lysates of O cells treated with 1 μM ATO or 1 μM APO for 72 h was performed using another anti-PML antibody, A301-168A-1 (a gift from Bethyl Laboratories), which can recognize the longest isoform, PML I, but not shorter PML isoforms such as PML VI and which has been proven useful for Western blot analysis. Consistent with the previous finding that ATO promotes PML degradation (70), the expression level of the PML I protein was lower in the ATO-treated O cells than in the APO-treated O cells (Fig. 4B), suggesting that PML degradation by ATO is associated with anti-HCV activity. To further examine whether PML is directly involved in the anti-HCV activity of ATO, we used lentiviral vector-mediated RNA interference to stably knock down PML in the O cells. To express an shRNA targeted to all PML isoforms (56), we used the VSV G-pseudotyped HIV-1-based vector system (1, 42, 71). We used the puromycin-resistant pooled cells at 10 days after the lentiviral transduction in this experiment. Immunofluorescence and Western blot analysis demonstrated a very effective knockdown of PML in the O cells (Fig. 4C and D). We quantitatively examined the level of HCV RNA in the PML knockdown O cells treated with or without either 1 μM ATO (Fig. 4E) or 1 μM APO (Fig. 4F) for 72 h. The results showed that the replication level of genome-length HCV-O RNA in the untreated PML knockdown cells was similar to that in control cells (Fig. 4E), suggesting that PML is dispensable in HCV RNA replication. Importantly, ATO effectively inhibited the HCV RNA replication in both the PML knockdown cells and control cells compared with that of the APO-treated cells (Fig. 4E and F). Thus, we concluded that PML was dispensable for the anti-HCV activity of ATO. Since the Chk2 checkpoint kinase has recently been implicated in ATO-induced apoptosis and in association with PML (27, 63, 64, 66), we examined the anti-HCV activity in the ATO-treated Chk2 knockdown O cells (3). As we previously described, Western blot analysis demonstrated very effective knockdown of Chk2 in O cells (Fig. 4G). Accordingly, we examined the level of HCV RNA in Chk2 knockdown cells treated with or without either 1 μM ATO (Fig. 4H) or 1 μM APO (Fig. 4I) for 72 h. Consistent with our recent finding that Chk2 is required for HCV RNA replication, the replication of genome-length HCV RNA in the untreated Chk2 knockdown cells was remarkably suppressed (Fig. 4H). However, ATO strongly inhibited the HCV RNA replication in the Chk2 knockdown cells compared with that in the APO-treated Chk2 knockdown cells (Fig. 4H and I), suggesting that Chk2 is not implicated in the anti-HCV activity of ATO.

Effect of ATO on the stress-signaling pathways. To date, the focus has been on PML and PML-retinoic acid receptor α as major targets of ATO (70). On the other hand, arsenic has been reported to modulate other cell-signaling pathways, especially stress-responsive transcription factors, such as nuclear factor κB (NF-κB), activator protein 1 (AP-1), and STAT3 (12, 37, 38, 62). Therefore, we examined the involvement of several stress-responsive pathways in the anti-HCV activity of ATO by luciferase-based reporter assays or Western blot analysis using an antibody which specifically recognizes STAT3 phosphorylated at tyrosine 705. Although it has been reported that ATO inhibited the NF-κB signaling pathway through a direct interaction with IKKβ at a high concentration (more than 10 μM) (29), neither 1 μM ATO nor 1 μM APO affected the endogenous NF-κB transcriptional activity in the present study (Fig. 5A and B). Conversely, ATO at least slightly stimulated mitogen-activated protein kinase kinase kinase (MEKK)-mediated NF-κB activation (Fig. 5A and B). Since NF-κB activation has been shown to stimulate HCV replication (60), the NF-κB pathway would seem not to be essential for the anti-HCV activity of ATO. Next, regarding the AP-1 signaling pathway, both ATO and APO are known to activate c-Jun N-terminal kinase (JNK) (45). Importantly, there was no stimulation of JNK activity at a dose below 30 μM (45). In fact, 50 μM ATO but not 50 μM APO strongly stimulates AP-1 activity by in-

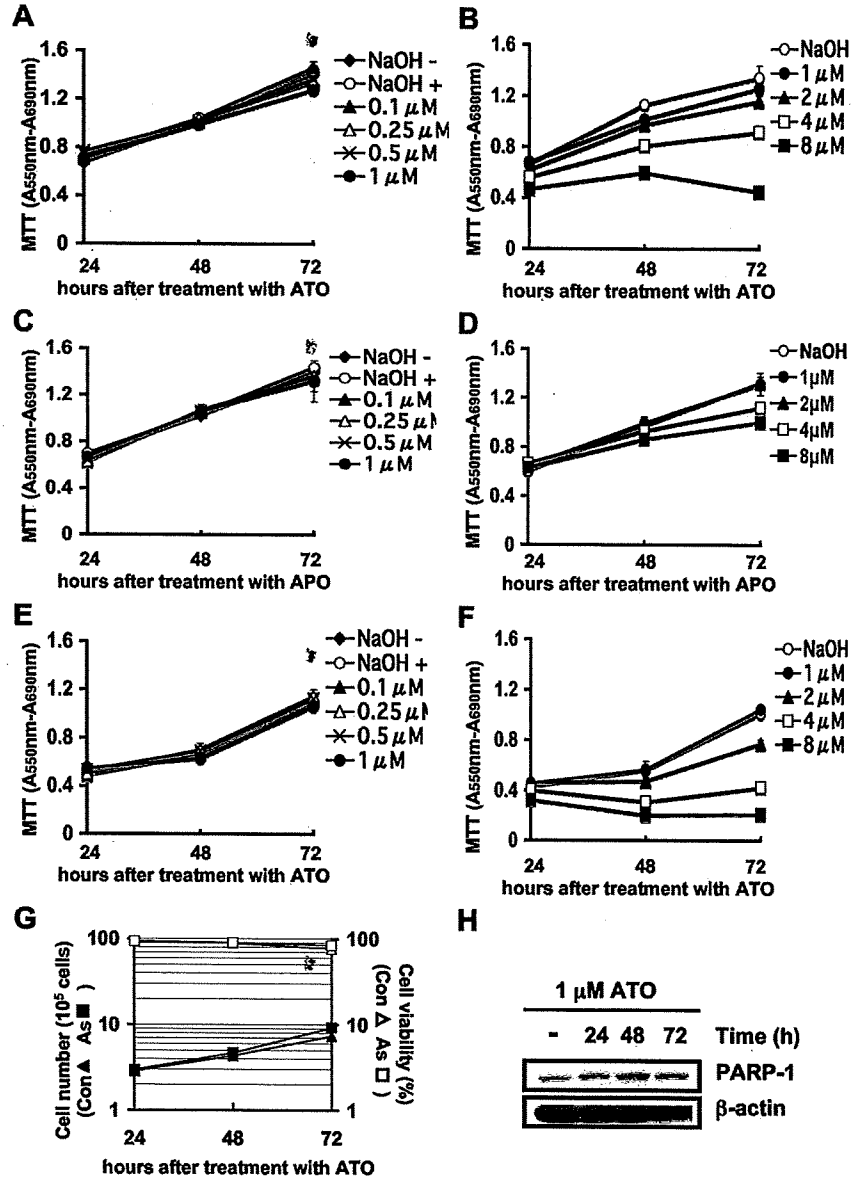

FIG. 3. Effect of ATO on cell growth and viability. (A and B) MTT assay of O cell lysates at the indicated times after treatment with ATO at various concentrations. NaOH (10 μM) was used as the solvent for ATO. The results shown are means from three independent experiments. Error bars indicate standard deviations. (C and D) MTT assay of O cell lysates at the indicated times after treatment with APO at various concentrations. (E and F) MTT assay of HuH-7 cell lysates at the indicated times after treatment with ATO at various concentrations. (G) Growth curve and viability of O cells after treatment with either 10 μM NaOH (Con) or 1 μM ATO (As). (H) Western blot analysis of cellular lysates with anti-PARP-1 or anti-β-actin antibody in O cells at the indicated times after treatment with 1 μM ATO.

hibiting a JNK phosphatase (10). Consistently, we found that both 1 μM ATO and 1 μM APO had a marginal effect on the AP-1 signaling pathway (Fig. 5C and D), suggesting that the AP-1 pathway is also not involved in the anti-HCV activity of ATO. Regarding the STAT3 signaling pathway, ATO has been reported to inhibit the phosphorylation of the STAT3 tyrosine at 705, leading to inactivation of the JAK-STAT signaling pathway (12, 62). In contrast, it has been reported that HCV constitutively phosphorylates and activates STAT3 (49, 59, 67). In this context, we observed constitutive tyrosine phosphorylation of STAT3 in untreated O cells (Fig. 5E). Furthermore, the marginal effect of 1 μM ATO on STAT3 phosphorylation and interleukin-6-mediated STAT3 activation was also observed (Fig. 5E and F). Taken together, these results at least suggest that the NF-κB, AP-1, and STAT3 pathways may not be associated with the anti-HCV activity of ATO at submicromolar concentrations.

The anti-HCV activity of ATO is associated with the glutathione redox system and oxidative stress. Finally, we focused on the involvement of the glutathione redox system and oxidative stress in the anti-HCV activity of ATO. For this, we analyzed the HCV replication level after combination treatment with ATO and antioxidants such as NAC and vitamin C using the OR6 assay system. When OR6 cells were treated with

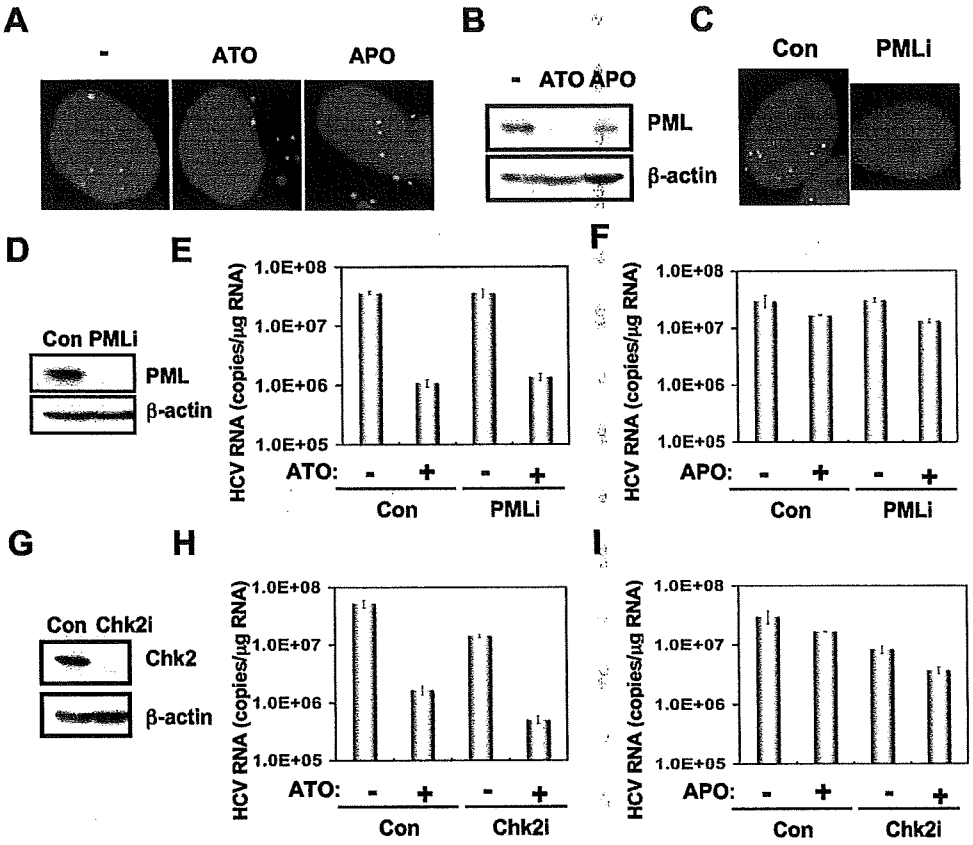

FIG. 4. PML and Chk2 are not required for the anti-HCV activity of ATO. (A) Subcellular localization of PML in O cells at 72 h after treatment with 10 μM NaOH (−), 1 μM ATO, or 1 μM APO. PML was detected by indirect immunofluorescence analysis with anti-PML antibody (PM001). DAPI staining of the nuclear DNA is also shown. (B) Induction of PML degradation by ATO but not by APO. The results of Western blot analysis of cellular lysates of O cells at 72 h after treatment with 10 μM NaOH (−), 1 μM ATO, or 1 μM APO with anti-PML (A301-168A-1) or anti-β-actin antibody are shown. (C) Stable knockdown of PML by shRNA-producing lentiviral vector in O cells. PML was detected by indirect immunofluorescence analysis with anti-PML antibody (PM001) in O cells expressing shRNA targeted to PML (PMLi) as well as in O cells transduced with a control lentiviral vector (Con). (D) Western blot analysis of cellular lysates with anti-PML (A301-168A-1) or anti-β-actin antibody in PML knockdown O cells (PMLi) as well as in control O cells (Con). (E and F) The level of genome-length HCV-O RNA was monitored by real-time LightCycler PCR in PML knockdown O cells (PMLi) as well as in control O cells (Con) after treatment with 10 μM NaOH (−), 1 μM ATO (+) (E), or 1 μM APO (+) (F) for 72 h. Results from three independent experiments conducted as described in the legend to Fig. 1A are shown. (G) Inhibition of Chk2 expression by shRNA-producing lentiviral vector. The results of Western blot analysis of cellular lysates with anti-Chk2 or anti-β-actin antibody in O cells expressing shRNA targeted to Chk2 (Chk2i) as well as in O cells transduced with a control lentiviral vector (Con) are shown. (H and I) The level of genome-length HCV-O RNA was monitored by real-time LightCycler PCR in Chk2 knockdown O cells (Chk2i) as well as in control O cells (Con) after treatment with 10 μM NaOH (−), 1 μM ATO (+) (H), or 1 μM APO (+) (I) for 72 h. Results from three independent experiments conducted as described in the legend to Fig. 1A are shown.

either 100 μM vitamin C or 10 mM NAC alone for 24 h or 72 h, the HCV replication was slightly enhanced (Fig. 6A and B), indicating that the antioxidant can activate HCV replication. Although the anti-HCV activity in the OR6 cells treated with 1 μM ATO and in combination with 100 μM vitamin C for 24 h was weakly reduced, 10 mM NAC completely and partially eliminated the anti-HCV activity of ATO after 24 h (Fig. 6A) and 72 h (Fig. 6B) of treatment, respectively, suggesting that oxidative stress and the glutathione redox system are associated with the anti-HCV activity of ATO. In contrast, the iNOS inhibitor 1400W did not suppress the HCV RNA replication or eliminate the anti-HCV activity of ATO, suggesting that NO is not involved in the anti-HCV activity of ATO (Fig. 6C). To further examine the involvement of oxidative stress in the anti-HCV activity of ATO, we examined ROS production in ATO-treated cells using two oxidative-sensitive fluorescent probes, DHE for detection of intracellular O_2^- and DCF for detection of intracellular H_2O_2. We found that 1 μM ATO could generate a significant level of intracellular O_2^- but not intracellular H_2O_2, while 2 μM BSO, an inhibitor of glutathione synthesis (14, 20, 33), could induce both O_2^- and H_2O_2 (Fig. 6D to H). Importantly, NAC diminished the ATO-dependent O_2^- induction (Fig. 6F). Since glutathione is a major antioxidant in cells and can clear away superoxide anion free radical, we also analyzed the changes of the intracellular glutathione level in ATO-treated O cells using CMF fluorescence, which can react with glutathione. As a result, we observed significant glutathione depletion in the cells treated with at least 1 μM ATO (Fig. 6I). To further confirm the involvement of glutathione in the anti-HCV activity of ATO, we examined the effect of cotreatment with ATO and BSO. When the OR6 cells were treated with 1 μM BSO alone, the HCV replication

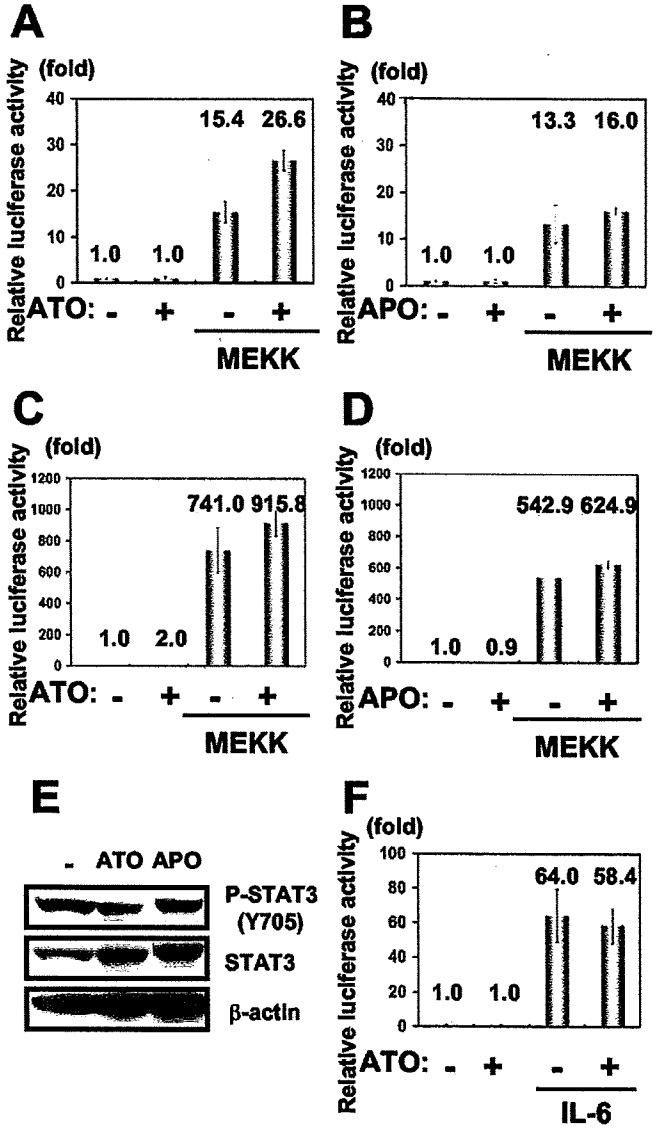

FIG. 5. Effect of ATO on the stress-signaling pathways. (A and B) Effect of ATO or APO on the NF-κB signaling pathway. O cells were transfected with 100 ng of reporter plasmid, pNF-κB-Luc, and/or 100 ng of pFC-MEKK (Stratagene, La Jolla, CA). Cells were treated with either 1 μM ATO (A) or 1 μM APO (B), and an FL assay was performed 24 h later. The results shown are means from three independent experiments. The relative FL activity is shown. (C and D) Effect of ATO or APO on the AP-1 signaling pathway. O cells were transfected with 100 ng of pAP-1-Luc and/or 100 ng of pFC-MEKK (Stratagene). Cells were treated with either 1 μM ATO (C) or 1 μM APO (D), and an FL assay was performed 24 h later as described for panels A and B. (E) Effect of ATO on the phosphorylation level of STAT3 at tyrosine 705. The results of Western blot analysis of cellular lysates with anti-phospho-STAT3 (Tyr705), anti-STAT3, or anti-β-actin antibody in O cells treated with either 1 μM ATO or 1 μM APO for 24 h are shown. (F) Effect of ATO on the STAT3 signaling pathway. O cells were transfected with 100 ng of STAT3 reporter APRE-Luc (41) (STAT3-Luc, a generous gift from T. Hirano, Osaka University, Japan). Cells were treated with 1 μM ATO for 19 h and then stimulated with 100 ng/ml of interleukin-6 for 5 h, and an FL assay was performed as described for panels A and B.

level was suppressed by about 30% compared with that of the control cells, and this occurred without cell toxicity (data not shown). However, consistent with previous reports in which ATO-induced apoptosis was enhanced by BSO (14, 20, 33), most of the cells died, possibly through apoptosis, when the OR6 cells were cotreated with 1 μM ATO and 1 μM BSO for 72 h (data not shown), suggesting that ATO and BSO synergistically generate ROS and deplete glutathione, resulting in induction of oxidative damage. Taken together, these results suggest that ATO may inhibit the HCV RNA replication by modulating the glutathione redox system and oxidative stress.

DISCUSSION

ATO has been reported to affect multiple biological functions, such as PML-NB formation, apoptosis, differentiation, stress response, and viral infection (38). Indeed, ATO has been shown to increase retroviral infectivity, including infectivity of HIV-1, HIV-2, feline immunodeficiency virus, simian immunodeficiency virus from rhesus macaques, and murine leukemia virus, although the mechanisms responsible for these changes are not well understood (5, 6, 32, 44, 47, 50, 57). PML, which is involved in host antiviral defenses, is required for the formation of the PML-NB, which is often disrupted or sequestered in the cytoplasm by infection with DNA or RNA viruses (17). The fact that ATO promotes the degradation of PML and alters the morphology or distribution of PML-NBs suggests that ATO enhances HIV-1 infection by antagonizing an antiviral activity associated with PML. In fact, HIV-1 infection has been reported to alter PML localization (57), although others have failed to confirm this finding (5). Furthermore, Berthoux et al. demonstrated that ATO stimulated retroviral reverse transcription (5). Moreover, ATO has been shown to have an inhibitory effect on host restriction factors, such as TRIM5a, Ref1, and Lv1, in a cell type-dependent manner (5, 6, 32, 44, 47, 50). In contrast, we have demonstrated that ATO strongly inhibited genome-length HCV RNA replication without cell toxicity (Fig. 1A and 2A). In addition, we observed the cytoplasmic translocation of PML in the HCV RNA-replicating O cells after the treatment with ATO (Fig. 4A). However, PML was dispensable for the anti-HCV activity of ATO as well as HCV RNA replication (Fig. 4E). In this regard, it is worth noting the recent report by Herzer et al. that the HCV core protein interacts with PML isoform IV and abrogates the PML function (22). Thus, PML may be involved in the HCV life cycle. In any case, the sensitivity to ATO and the cellular target of ATO seem to be different between HCV and HIV-1.

HCV infection has been shown to cause a state of chronic oxidative stress like that seen in chronic hepatitis C, which may contribute to fibrosis and carcinogenesis in the liver (16, 18, 40). In particular, HCV replication has been associated with the endoplasmic reticulum (ER), where HCV causes ER stress. Indeed, HCV NS5A and core, the ER-associated proteins, have been reported to trigger ER stress (4, 55). Therefore, HCV infection causes production of ROS and lowering of mitochondrial transmembrane potential through calcium signaling (4, 36). Among the HCV proteins, core, E1, NS3, and NS5A have been shown to be potent ROS inducers, and these HCV proteins also alter intracellular calcium levels and induce oxidative stress, thereby inducing DNA damage, and constitu-